HIGH-FREQUENCY UNDERWATER SOUND

INTRODUCTION

We are all familiar with sound effects such as the delay in the echo from a far-off canyon wall, the continually changing pitch in the sound of a passing train, or the distinct sound of an empty room versus one filled with furniture. Such sounds carry information about the environment, objects within it, and sources of the sound. In the underwater environment, sound, which is energy in the form of a pressure wave, replaces light and other forms of electromagnetic wave energy (such as microwaves or radar) as the paramount means to gather information. Attenuation of acoustic waves is relatively low in water allowing the underwater environment to be more transparent to sound energy. On the other hand, light and other electromagnetic waves are absorbed strongly by water, and thus the underwater environment is more opaque to electromagnetic wave energy.

This article will focus on some applications of *high-frequency* sound to probe the underwater environment. We define high-frequency somewhat broadly, meaning frequencies of order 10^4 Hz (10 kHz) up to about 10^7 Hz (10 MHz). The nominal upper frequency limit again is chosen from the applications point of view. Only a few applications of underwater sound use frequencies greater than about 10 MHz, because underwater sound at these very high frequencies will, like electromagnetic energy, be absorbed over a very short distance. Sound absorption remains an important controlling factor for the 10^4–10^7-Hz frequency band as well. For example, for a frequency of 10 kHz, sound travels in seawater about 10 km before its amplitude is reduced significantly because of absorption; when the frequency is 1 MHz, this distance reduces to about 30 m.

The sound frequency f, wavelength λ, and phase speed c are related by $\lambda f = c$. Also, one can define a wavenumber k and angular frequency ω with

$$\omega = 2\pi f = kc \tag{1}$$

In seawater, c is nominally 1500 m/s (but may vary considerably with depth as discussed later), and the frequency range 10 kHz to 10 MHz translates to underwater sound wavelengths of order 10 to 10^{-3} cm.

Both sound wavelength and the distance over which sound travels specify the manner in which sound is used in the underwater environment. Just a few examples of the diverse applications of high-frequency underwater sound include remote sensing of plankton, fish populations, and other oceanographic properties (1); depth sounding in coastal waters, high-resolution mapping of the seafloor, and underwater navigation (2, 3); studies concerning properties of the seafloor (4); and underwater communication and telemetry (5). Many of these applications are covered by the familiar acronym "sonar," which stands for *s*ound *n*avigation *a*nd *r*anging. Looking ahead, this article's emphasis is on remote sensing of water column properties, but the topics introduced also pertain to the broader use of high-frequency underwater sound.

With this article limited to underwater at high frequencies, we necessarily pass over the set of diverse applications that rely on lower frequency underwater sound. For example, forward-looking sonars aboard military submarines and ships, downlooking sonars to measure ocean depths, and side-scan sonars used in large-scale bathymetric surveys use frequencies in the 1-kHz to 10-kHz band. When the frequency is less than about 1 kHz, sound can travel several hundred kilometers before losing its energy to the surrounding environment. At still lower frequencies ($\sim$100 Hz) the ocean becomes nearly transparent to sound. Experiments in ocean acoustic tomography (6) are conducted in this frequency band, wherein precise measurements of the travel time for sound travel over thousands of kilometers of ocean are used to infer the mean properties of the intervening ocean, such as the average temperature of the ocean. Low-frequency sound also penetrates deep into the seabed (7, 8), and experiments using low-frequency sound are designed specifically to measure properties of the seabed (9).

In the sections ahead we discuss high-frequency underwater sound in relation to the following topics: sound waves in fluids; the decibel scale; underwater transducers, calibration techniques and cavitation; propagation in heterogeneous media; absorption; reflection from boundaries; scattering from bubbles, zooplankton, and turbulent microstructure; and underwater imaging.

SOUND WAVES IN FLUIDS

Sound waves in fluid are longitudinal (compressional) waves, meaning that in the presence of a sound wave, a parcel of fluid moves back and forth with a particle velocity $\boldsymbol{u}$ that is aligned with the direction of the propagating sound wave. A region of alternating pressure results in slightly higher than the ambient static pressure p_0 when the parcels compress and slightly lower than p_0 when the parcels spread out. The sound pressure p is the pressure difference from p_0. Accompanying the changing pressure is a minute change in density ρ equal to the density difference from the fluid's ambient density ρ_0. The three primary *acoustic field variables* are thus p, ρ, and $\boldsymbol{u}$.

The *linear theory* of sound waves (see, for example, References (10–12)) usually is sufficient to predict many of the acoustical effects encountered in applications of high-frequency underwater sound. The key assumption in linear theory concerns the relative smallness of the variables p, ρ, and $\boldsymbol{u}$, and that there is a linear relation among them. The assumption that $\rho/\rho_0 \ll 1$ leads to the linearized acoustic equation of state $p = \rho_0 c^2$. For this linear approximation to apply, the restriction on the acoustic pressure is such that $p \ll \rho_0 c^2$ (13). Similarly, the restriction on $\boldsymbol{u}$ is $|\boldsymbol{u}|/c \ll 1$, where the ratio $|\boldsymbol{u}|/c$ is the acoustic Mach number. To see how the smallness assumption is easily satisfied, take the maximum acoustic pressure 1 m in front of a typical research sonar to be 10^4 N/m^2. Taking ρ_0 for seawater as 1025 kg/m^3, then $\rho_0 c^2 = 2.3 \times 10^9$ N/m^2, and $|p|/\rho_0 c^2 \sim 4 \times 10^{-6}$. Moving farther away from the

sonar by a factor of 10 reduces this ratio by a factor of 10.

We remark that the main focus of this article concerns the longitudinal sound waves that exist in fluids. However, in reflection and scattering from solid objects, including the seabed, there also can be transverse waves for which $\boldsymbol{u}$ is perpendicular to the direction of the propagating sound wave. The relationship between the longitudinal sound speed c_L and transverse sound speed c_T is given by

$$\frac{c_L}{c_T} = \sqrt{\frac{2(1-\nu)}{1-2\nu}} \tag{2}$$

where ν is Poisson's ratio, which lies in the range 0 to 0.5 for typical elastic materials (14). For a fluid $\nu = 0.5$, for aluminum $\nu = 0.3$, and for steel $\nu = 0.23$. For sound waves in fluids, c_T is zero; there is no need to employ the subscript in c_L, and instead we write just c for sound speed.

The acoustic variables p, ρ, and $\boldsymbol{u}$ are described by functions that satisfy the acoustic wave equation plus boundary conditions (e.g., see References 1, 7, and 11–18). In the underwater environment, boundary conditions are imposed by the sea surface, the seabed, and submerged objects from which sound can be reflected.

A simple form of the wave equation describing the pressure field in three dimensions is one that governs a spherically symmetric wave. Such a field would result from a harmonically pulsating sphere of radius a, with pressure as a function of time t and range from source the origin of the sphere r given by

$$p(t, r) = \frac{A}{r} e^{i(kr-\omega t)} \tag{3}$$

where the complex amplitude A is given by

$$A = a\left(\frac{ka}{ka+i}\right)\rho_0 c u_o e^{-ika} \tag{4}$$

In equation 4, u_o is the amplitude of the radial velocity at the surface of the sphere, and a harmonic time dependence of $e^{-i\omega t}$ is assumed. The real part of equation 3 is taken to relate to physical measurements of pressure, e.g., as obtained by a transducer.

The ratio of acoustic pressure to acoustic particle velocity in the medium is the specific acoustic impedance Z. For a spherical wave acoustic particle velocity is only in the radial direction, and so we drop the vector notation, $\boldsymbol{u}$ writing as a scaler, i.e., u, and $u\ (t, r) = p(t, r)/Z$, where Z is given by

$$Z = \rho_0 c \frac{kr}{kr+i} \tag{5}$$

Notice that at ranges described by $kr \gg 1$, Z becomes purely real and equal to the quantity $\rho_0 c$, which is the *characteristic acoustic impedance*. This region is known as the acoustic *far field* (11–13), and here p and u are in phase with each other such that efficient sound radiation takes place, with the "radiation load" presented by the underwater medium being $\rho_0 c$. The analogy to electric fields is evident where p corresponds to voltage, u to current, and Z to electrical impedance.

Equations 3–5 provide much insight into the nature of acoustics sources and propagation. First, a key property shown in equation 4 is that the amplitude of the source is a linear function of u_o. Second, both non-dimensional parameters ka and kr have now entered the picture. The first represents the size of the acoustic source scaled by wavelength, and the second represents a propagation range scaled by wavelength. A remarkable amount of predictive information can be determined from these parameters.

The acoustic intensity gives the time average of the power flowing through a unit area and is given by ½ Real($p\ u^*$). For the spherical source and the case $kr \gg 1$, the intensity I equals $\frac{1}{2}|\mathrm{A}|^2/(r^2\rho_0 c)$ and this quantity goes as $\sim 1/r^2$, which is known as the *inverse-square law*. The total power radiated from the pulsating sphere is given by $2\pi|\mathrm{A}|^2/(\rho_0 c)$. Looking at this quantity more closely, we observe that the total power goes as $2\pi a^2 \rho_0 c|u_o|^2(ka)^2$ for $ka \ll 1$ and, all else being equal, the radiated power is considerably smaller for diminishing ka. It is for this reason that it is difficult to radiate significant amounts of acoustic power from a small acoustic source. For $ka \gg 1$, the radiated power goes as $2\pi a^2 \rho_0 c|u_o|^2$ and is independent of ka.

Considering now some small region of interest located in the far field, the acoustic wave fronts assume the properties of a *plane wave* (15), insofar as the spherical wave fronts become locally planar. The amplitude is decreasing with r, but at a rate much slower than the phase, and the local amplitude is set by the range r associated with the region of interest. The expression for such a plane wave traveling at angle θ with respect to the x-axis is

$$p = A e^{i(kx\cos\theta + kz\sin\theta - \omega t)} \tag{6}$$

Here, complex constant A assumes the dimensions of pressure (and dependence on a third dimension is suppressed for simplicity). For a plane wave, acoustic particle velocity and pressure again are related through Z, but Z is now real and equal to $\rho_0 c$. A propagation *vector* $\boldsymbol{k}$ is identified with x, z components equal to $k\cos\theta$ and $k\sin\theta$, respectively, pointing in the plane wave's single direction of propagation and normal to the wave's planar wave fronts. Later, in the context of propagation in media with a gradually changing sound speed, we will see how the wave vector may change its direction, and the trajectory of these changes defines an *acoustic ray*.

THE DECIBEL SCALE

Acoustic variables ordinarily will vary over several orders of magnitude, and it is often convenient to express this huge variation through a logarithmic scale. The decibel (abbreviated as dB) scale for intensity is defined by

$$\text{Value in dB} = 10\log(I/I_{\text{ref}}) \tag{7}$$

where log is base 10 and I_{ref} is a reference intensity used to relate the decibel equivalent of intensity I back to absolute linear intensity units. In underwater acoustics, it is standard practice to set I_{ref} equal to the intensity of a plane wave with an rms pressure of 1 micropascal (μPa), which is equivalent to 10^{-5} dynes/cm^2. When we take $\rho_0 c$ of seawater to be 1.5×10^5 dynes s/cm^3, this sets I_{ref} equal to

0.67×10^{-22} W/cm^2. Were the intensity I to equal I_{ref}, then its decibel value would be given formally as 0 dB re 1 μPa, which is shorthand for 0 dB with reference to the intensity of a plane wave with a rms pressure of 1 μPa.

The decibel scale can be used for any acoustic variable proportional to either power or intensity. Thus, to find the decibel equivalent of acoustic pressure, one must first square the pressure or equivalently compute

$$L_p = 20 \log(p/p_{\text{ref}}) \tag{8}$$

where L_p means "pressure level." (It is standard practice to use capital letters for decibel variables and refer to them as a "level.") The reference pressure is again 1 μPa rms, and therefore, p also must be rms and not, say, peak pressure. For example, using the previous example of peak pressure equal to 10^4 N/m^2 at range 1 m from the sonar, then the equivalent rms pressure expressed in μPa is 0.707×10^{10} μPa, and thus, $L_p = 197$ dB re 1 μPa. At a range of 10 m, the pressure amplitude is reduced by a factor of 10 compared with the amplitude at 1 m because of spherical spreading, and L_p decreases to 177 dB re 1 μPa. Often the decibel is used just to relate two quantities, without regard to reference. For example, the difference between two pressures, say p_{A} and p_{B}, is expressed through 20 log of the ratio, $p_{\text{A}}/p_{\text{B}}$, giving the difference in these pressures in terms of decibels.

UNDERWATER TRANSDUCERS

An acoustic transducer is a device that converts an electric signal, such as voltage, into a pressure signal that propagates as a sound wave. Transducers are reciprocal devices, so they also carry out the reverse task of sound-to-electric conversion. (The term "hydrophone" applies to a device used only for sound-to-electric conversion.) The most common conversion mechanism in underwater transducers is the piezoelectric effect, in which the transducer material is deformed slightly when a voltage is applied across attached electrodes. These deforming vibrations produce a time-dependent pressure field in the water $p(t)$, which propagates as a sound wave. In a like manner, a voltage signal $v(t)$ is produced by the transducer (or hydrophone) when it is subjected to the pressure fluctuations of a sound field, which also slightly deforms the transducer material.

Modern piezoelectric materials used in transducers most often consist of ceramic compositions such as barium titanate ($BaTiO_3$), lead zirconate titanate (PZT), and PVDF (16, 17). A typical configuration for the piezoelectric ceramic material is a thin circular plate of thickness L, where L is between $\lambda/2$ and $\lambda/4$ (16). The transducer vibrations occur in the thickness dimension, with the resonant frequency of the transducer (f_0) being approximately proportional to L^{-1}. The exact f_0 depends on the particular piezoelectric material, how it is encased in the transducer housing, and how the transducer is networked together with system electrical components such as the driving amplifier and possible tuning circuitry. The transducer operates most efficiently within a frequency band centered around f_0, and the transducer's operational bandwidth is defined by $f_2 - f_1$, where f_1 and f_2 are, respectively, the frequencies below and above f_0 at which the transducer output acoustic power has fallen to 50% of maximum. The transducer Q value is defined as $f_0/(f_2 - f_1)$, with a typical Q value being about 10.

Ultimately, the transducer converts electric power Π_{E} to acoustically radiated power Π_A with a degree of efficiency ε (a typical ε ranges between 0.4 and 0.8), such that $\Pi_A = \varepsilon \Pi_E$. If the transducer were to radiate acoustic power uniformly in all directions, then

$$\Pi_A = I_0 4\pi r_0^2 \tag{9}$$

where I_0 is acoustic intensity (W/m^2) at range r_0 (m) from the transducer face. We set r_0 equal to 1 m, which is the standard reference distance in underwater acoustics. Transducers that operate in this manner are known as *omnidirectional transducers*. For example, a spherical source would radiate as an omnidirectional transducer. However, most applications of underwater ultrasound require *directional* transducers that concentrate the transmitted acoustic power into a specific direction, as into an approximate cone of solid angle Ψ. Given that the transducer is reciprocal, then it also will preferentially receive sound coming from within this same directional cone and will largely be insensitive to sound coming from other directions. This property is described by the transducer's intensity pattern function $b(\theta, \phi)$ (or beam pattern for short), which is proportional to the sound intensity transmitted into, or received from, directions described by angles θ and ϕ. For a circular piston transducer of diameter d, the theoretical beam pattern is (17)

$$b(\theta) = \left| \frac{2J_1[(\pi d/\lambda)\sin\theta]}{(\pi d/\lambda)\sin\theta} \right|^2 \tag{10}$$

For such transducers, b is symmetric about a central axis normal to the transducer face, or *acoustic axis*, and thus, the beam pattern is described completely by only one angle. Figure 1 shows the measured $b(\theta)$ for a circular piston transducer with a diameter d of 43 mm and a center frequency of 108 kHz plotted against the theoretical $b(\theta)$ based on equation 10. Note that both curves are plotted in a decibel scale, since $b(\theta)$ is equal to the ratio of intensity transmitted at angle θ to the intensity transmitted along the acoustic axis, or $I(\theta)/I(0)$. In this example, good agreement between the two curves occurs only in the main-lobe region. Within the side-lobe region, deviation from ideal, theoretical behavior is common because the beam pattern in this region is more sensitive to the precise mechanical coupling between the piezoelectric disk material and its mounting within the transducer housing. However, the main lobe is by far the most important, and transducers are often classified by the angular width of their main lobe. A common definition is that of the beam pattern's angular width between points that are reduced by 3 dB from that of the maximum on the acoustic axis. For the circular piston transducer, this width in degrees is well approximated by

$$\theta_{3dB} \approx 60\,\lambda/d \tag{11}$$

The important parameter ka discussed in the context of the radiating spherical source emerges here as well. For

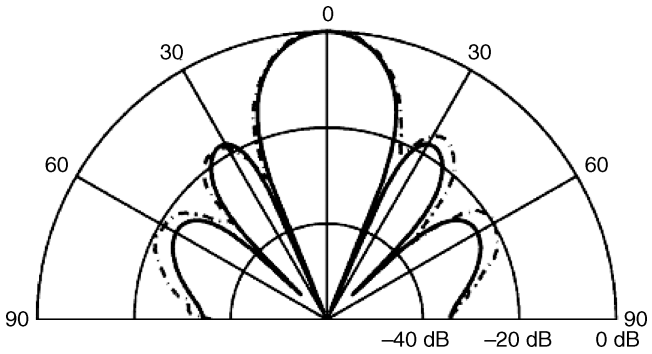

Figure 1. Measured (dashed line) and theoretical (solid line) curves representing $b(\theta)$ for a circular piston transducer with a diameter of 43 mm and a center frequency of 108 kHz.

example, call a the radius of piston and an equivalent expression for beam pattern angular width is readily found, with the width going as $1/ka$. Thus, for $ka \ll 1$, any transducer behaves as a spherically symmetric source insofar as the angular width now becomes very large.

The beam pattern as shown in Fig. 1 is valid only at ranges r from the transducer that are in the transducer's far field or Fraunhofer zone. For a circular piston transducer of radius a, the far field is delimited by the critical range $\pi\, a^2/\lambda$ (15, 17), which also is known as the *Rayleigh range*. The zone at ranges less than $\pi\, a^2/\lambda$ is called the near field, or Fresnel zone, of the transducer. Here, sound intensity varies rapidly with distance because of the interference of sound radiation coming from different surface elements of the transducer (1, 18).

The concentration, or focusing, of acoustic power into a beam is quantified by the ratio sometimes called the *directivity factor* (3, 17)

$$\text{Directivity factor} = 4\pi/\int b(\theta, \phi) d\Omega \tag{12}$$

The numerator in equation 12 represents $b(\theta, \phi)$ for an omnidirectional transducer, integrated over 4π steradians of solid angle. The denominator represents the same operation using $b(\theta, \phi)$ from a directive transducer. If we use b from a circular piston transducer of diameter d, the denominator reduces to the evaluation of

$$2\pi \int_{-\pi/2}^{\pi/2} b(\theta) \cos\theta \, d\theta \approx \frac{4\lambda^2}{\pi d^2} \tag{13}$$

and thus, the directivity factor is approximately $(\pi d/\lambda)^2$. Urick (3) provides useful approximate expressions for the directivity factor of common transducer geometries. The *directivity index*, DI, is defined as 10 log of the directivity factor and is therefore equivalent to 10 log of the ratio (I_d/I_{omni}), where I_d is the intensity radiated from a directive transducer along its acoustic axis and I_{omni} is the intensity radiated from an omnidirectional transducer with the same total acoustic power. A typical DI is 30 dB, meaning that the concentration of acoustic power by the directive transducer has produced a 1000-fold increase in acoustic intensity.

Calibration Techniques

Transducer calibration usually means quantifying in absolute terms the transducer's ability to convert voltage to pressure (transmit voltage response) and convert pressure to voltage (receive voltage response), plus determining the transducer's beam pattern $b(\theta, \phi)$. (There are other descriptors of transducer performance, such as input current-to-pressure response and overall transducer efficiency. Depending on the transducer application, these may or may not be determined explicitly.) It is very difficult to obtain reliable estimates of key transducer properties from theoretical calculations. The one exception is the beam pattern, where for simple transducer shapes, such as a circular piston, equations like equation 10 provide a good approximation. But, as Fig. 1 illustrates, equation 10 represents an idealized beam pattern for a circular aperture, and a real transducer beam pattern will show differences particularly in the side-lobe region that are revealed only through an actual measurement.

The transducer's *transmit voltage response*, or TVR, relates the input voltage to the output acoustic pressure of a transducer, which usually will be a function of frequency. The TVR is expressed in decibels; for example, at a given frequency, say 50 kHz, a typical value is 180 dB re μPa/Vrms, which means that when a 1-V rms sinusoidal signal of frequency 50 kHz is applied to the transducer leads, a pressure signal of the same frequency is generated that will have an rms pressure of 180 dB re 1 μPa at a distance 1 m from the transducer face. Similarly, The transducer's *receiving voltage sensitivity*, or RVS, relates the input acoustic pressure signal to transducer output voltage. A RVS for a typical research sonar at frequency 50 kHz is -120 dB re Vrms/μPa. The interpretation here is that an acoustic pressure signal of rms amplitude equal to 1 μPa produces an output rms voltage equal to 10^{-6} V or -120 dB re 1 Vrms. Such a small pressure would never be recorded, as underwater ambient noise in the neighborhood of 50 kHz would place the rms voltage closer to 10^{-3} V or greater (for 1-kHz bandwidth). Still, the RVS number applies to higher acoustic pressures as we assume a linear relation between pressure and voltage just as with the TVR number.

Transducer calibration techniques fall into three basic categories; the first two are discussed at length by Bobber (19) [see also Urick (3) and Stansfield (17)], and the third is discussed by Foote (20).

1. Comparison Method
   Properties of the unknown transducer are compared with those of a previously calibrated, or standard, transducer. The U.S. Navy maintains several standard transducers for calibration that can be leased to other facilities. For example, the University of Washington's Applied Physics Laboratory acoustic test facility uses Navy standard transducers for calibration standards.
2. Reciprocity Method
   The principle of reciprocity states that the transducer's receiving response in terms of pressure-to-output voltage is related to the transducer's

transmitting response in terms of input current to pressure. Use of reciprocity thus allows calibration of transducers without use of a standard transducer.

3. Calibration Sphere Method
   The echo from a solid sphere is used to calibrate the transducer. It is well known that accurate values for the echo amplitude from a sphere can be obtained through theoretical computations. For calibration purposes, the key is using a proper sphere diameter and material to avoid having strong resonant scattering effects included in the sphere's echo. For example, to calibrate 38-kHz echo sounders such as those used in fisheries research, a 60-mm-diameter copper sphere is recommended. Spheres made of tungsten carbide also are used for frequencies between 50 kHz and 500 kHz.

Continuing with the above example for which TVR equals 180 dB re μPa/Vrms, if the transducer is driven by a 10-Vrms signal, then the pressure level L_p equals 200 dB re 1 μPa at range of 1 m were this measurement to be on the transducer maximum response axis (MRA), i.e., where $b(\theta, \phi)$ is maximal. Along this same axis we anticipate L_p to be 194 dB at a range of 2 m from the transducer. The pressure level measured at the standard range of 1 m is known as the transducer's *source level* (21), abbreviated as *SL*. Recapitulating the foregoing remarks on decibel quantities and references, a source level of 200 dB means the rms pressure is 10^{10} μPa (10^4 Pa) at range of 1 m from the transducer along its MRA, and intensity is $(10^4 \text{ Pa})^2/\rho_0 c$, or 67 W/m^2.

Extra care must be taken to ensure consistency in the units when examining the acoustic power Π_A radiated by the transducer. Note first that an intensity I_0 defined at range 1 m (r_0) of $(1\ \mu\text{Pa})^2/\rho_0 c$ equates to 0.67 10^{-18} W/m^2. If this intensity were radiated omnidirectionally, then the total radiated power would be $I_0 4\pi r_0^2$ equivalent to -170.8 dB re 1 W. Recall that for a directive transducer, the power is concentrated within a beam as quantified by the directivity index DI. The total power radiated by a directive transducer given the same I_0 is -170.8 – DI in dB re 1 W. We thus arrive at the very handy decibel relation between radiated acoustic power Π_A (which also can be found by $\varepsilon\ \Pi_E$) and source level:

$$SL = 10\log(\Pi_A) + DI + 170.8 \tag{14}$$

Cavitation

Cavitation will occur if the peak amplitude of the acoustic pressure p approaches the hydrostatic pressure p_0. With the acoustic pressure being sinusoidal, then $p + p_0$ can take on negative values. Bubbles, or cavities, form in the evacuated negative pressure regions, causing the transducer performance to degrade significantly in terms of linearity and radiation efficiency (3, 17). Erosion damage can occur at the transducer face where bubbles preferentially form.

The onset of cavitation is determined by the *cavitation threshold* pressure. Close to the sea surface, p_0 is about to 1 atm or 10^{11} μPa; thus, a very rough estimate of the cavitation pressure threshold p_c is when the peak acoustic pressure amplitude reaches 1 atm or a pressure level of about 217 dB re 1 μPa based on rms pressure. In fact this threshold will be somewhat higher. The cavitation threshold must increase as the operating depth increases because of the increase in hydrostatic pressure. But also a time scale is involved for the onset of cavitation; with increasing frequency, the actual time of the negative pressure decreases, which also pushes up the cavitation threshold. Smith (22) summarizes these two effects into an empirical formula based on published data from various experiments to measure the cavitation threshold versus frequency (see also References 3 and 15). The result is

$$L_c = 20\log[1 + (z/10) + (f/36)^2] + 220 \tag{15}$$

where L_c is the cavitation threshold in dB re 1 μPa, z is depth in m, and f is frequency in kHz. As a specific example, L_c is about 229 dB re 1 μPa for a 30-kHz sonar operating within about 10 m from the sea surface, and therefore, the sonar's *SL* should not exceed this value.

PROPAGATION IN HETEROGENEOUS MEDIA

Thus far we have assumed a constant, 1500 m/s, to represent a nominal speed of sound underwater. This number is representative of the sound speed in the upper 10 m of ocean at mid-latitudes. Nominal values for sound speed often are sufficient to handle many applications of high-frequency underwater sound involving short range, say on the order of 10 m. But when longer ranges are involved, it is necessary to account for the spatial and sometimes temporal variation in sound speed. The speed of sound underwater varies with temperature, salinity, and static pressure. A simplified empirical expression relating these quantities is (1)

$$\begin{aligned} c = {} & 1449.2 + 4.6T - 0.055T^2 + 0.00029T^3 \\ & + (1.34 - 0.01T)(S - 35) + 0.016z \end{aligned} \tag{16}$$

where T is temperature (°C), S is salinity (parts per thousand), and z is depth (m). The depth-varying sound speed caused by temperature and salinity variation, plus the influence of increasing pressure with depth, determines in large part the nature of underwater sound propagation.

Ray theory (3,7,8) is an approximate approach for handling wave propagation in heterogeneous media, and it is well suited for high-frequency underwater sound. The validity of the ray theory hinges on the medium being slowly varying with respect to a spatial coordinate. For example, taking the variation in c with depth, a necessary but not sufficient condition (8) for the medium to be slowly varying is

$$\frac{1}{\omega}\left|\frac{dc(z)}{dz}\right| \ll 1 \tag{17}$$

For increasing frequency, this condition becomes easier to satisfy.

To understand ray theory, we first invoke the aforementioned plane wave approximation and assume that the acoustic pressure is described by a plane wave as in equation 6. Let this plane wave be initially propagating in a

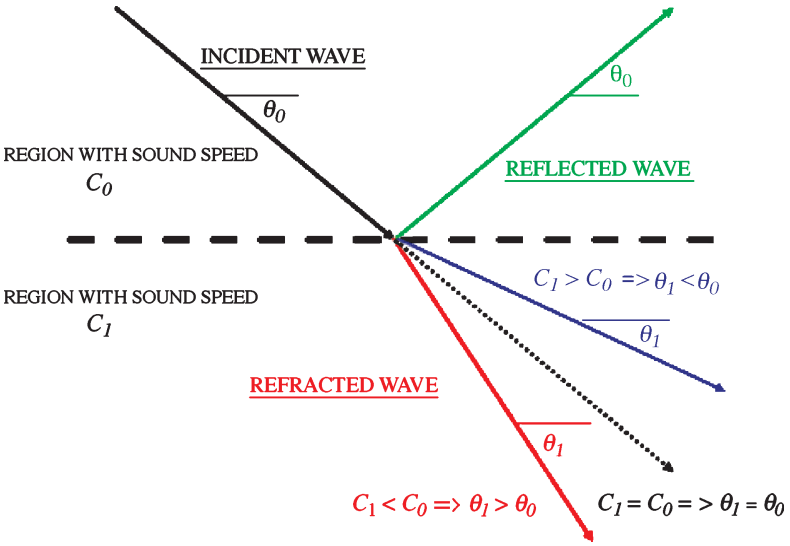

Figure 2. Example of Snell's law showing a ray representing a plane wave in region with sound speed c_0 (black arrow) entering a second region with sound speed c_1. Depending on the relation between c_0 and the ray will undergo downward refraction (red arrow), upward refraction (blue arrow), or no refraction (dashed, black arrow). A reflected ray (green arrow) also is shown.

medium with sound speed c_0 and then cross into another region of water with sound speed c_1. The ray representing the plane wave in the c_0 medium is shown by the solid, black arrow in the upper half of Fig. 2. Upon crossing the boundary separating the two media, θ_0 changes to θ_1 according to Snell's law

$$\frac{\cos\theta_0}{c_0} = \frac{\cos\theta_1}{c_1} \tag{18}$$

which is one of the most useful expressions in the study of wave propagation. Upward refraction of the plane wave occurs if $c_1 > c_0$ (blue arrow), downward refraction occurs if $c_1 < c_0$ (red arrow), and no refraction occurs if $c_1 = c_0$ (dashed, black arrow).

Note that Snell's law applies exactly to the situation in Fig. 2, which also shows a ray reflected from the interface (green arrow), and is discussed in the following section. We assume that such reflections are negligible in the following illustration of wave propagation through a medium of depth-varying sound speed, which is a very reasonable assumption provided that the sound speed undergoes gradual change in the manner of equation 17.

Consider next a continuously varying sound speed as a function of depth approximated by layers of differing constant speed. Snell's law in this case governs the refraction at the interface between each layer, and in the limit of vanishingly small layer thickness, Snell's law for a continuous sound speed profile $c(z)$ becomes

$$\frac{\cos\theta(z)}{c(z)} = \text{ray parameter} \tag{19}$$

In ray theory, a ray follows the trajectory of a wave vector, whose direction may vary continuously within a medium of continuously varying sound speed. The constant in equation 19 is known as the *ray parameter*, which is a value conserved by an individual ray as it refracts within a horizontally stratified medium. It is the basis for computing ray diagrams that show the paths taken by sound as it propagates through a medium with spatially varying sound speed.

If the sound speed profile $c(z)$ contains a local minimum, an *acoustic channel* is formed at the depth corresponding to the minimum sound speed. If a sound source were placed at or near this depth, then a ray issued from the source with negative launch angle with respect to horizontal refracts upward, conserving its ray parameter according to equation 19. For example, if the initial angle θ_0 is a small angle, then $\theta(z)$ can eventually reach 0°, and the ray will begin upward travel back toward the sound speed minimum. Upon reaching the ray's starting depth, its angle is now the same absolute value as θ_0 but now positive and the ray arches back toward the sound speed minimum in the same manner. The result is alternating downward and upward refraction, which traps, or channels, the ray as it cycles between the upper and the lower boundaries of the channel. With sound energy now confined, it diverges cylindrically, as $\sim 1/r$, rather than spherically as $\sim 1/r^2$, allowing sound to travel to much longer ranges. The depth at which the minimum sound speed occurs is the *sound channel axis*. A striking example of this effect is the deep sound channel, or SOFAR channel (e.g., see References 3–8). It is formed at a depth of roughly 1000 m, where the ocean's temperature approaches a constant of about 4 °C. The sound speed is decreasing with increasing depth to this point, and at ~1000 m, it begins increasing from the influence of hydrostatic pressure.

The SOFAR channel represents one example of the behavior of underwater acoustic channels, or *waveguides* (7, 8). Another consequence of refraction is the focusing and defocusing of sound energy, which can modify further either cylindrically or spherically decaying acoustic fields. To see how this occurs, consider the sound speed versus depth profile:

$$\begin{aligned} c(z) &= 1501, & z \le 65\text{m} \\ c(z) &= 1522 - gz & z > 65\text{m} \end{aligned} \tag{20}$$

where the sound speed gradient g equals 0.323 s^{-1}. This equation is an approximate fit to sound speed measurements made during an experiment conducted about 400 nautical miles off the California coastline during winter conditions (23) (the equation applies only to depths less

than about 200 m). The upper isospeed layer is known as a mixed layer; here turbulent mixing from winter storm activity has homogenized the temperature and salinity of the water column, producing a more uniform sound speed that we represent as a constant. Underneath the mixed layer starting at about 65 m, the thermocline leads to a steady decrease in sound speed modeled by a linear function with rate g. These two canonical sound speed regimes, isospeed and linear gradient, illustrate many of the key effects of sound refraction in the ocean.

Now consider a sound source placed at depth 150 m and a receiver at depth 60 m that is 1000 m downrange. By simple application of equations 19 and 20, a ray originally leaving the source with a grazing angle of 10° will have assumed a grazing angle of 5.4° when it reaches a depth of 100 m, and 0° at 80 m. At this point the ray curves downward, having reached a vertex, and will begin a steady downward travel causing it to miss the receiver completely. It is easy to show (e.g., see References 1, 3, and 7) that the ray's trajectory is exactly circular while traveling within a linear gradient, with radius of curvature $R_c = c_v/g$, where c_v is the vertex sound speed of the ray, equal to 1496.28 m/s for the ray with 10° launch angle.

A collection of rays issuing from the source is shown in Fig. 3 (called a "ray fan"); these rays show the direction of energy propagation for this combination of source depth, range, and $c(z)$. Shown in Fig. 3 are the subset of rays with launch angles between 9° and 16° (every 0.5°). Refraction within the linear gradient region has turned rays with launch angle less than about 11° downward, with trajectories that miss the receiver completely. Rays with launch angles greater than about 12° eventually reach the upper isospeed layer, and they continue propagating within this layer with unchanging direction until they reach the sea surface, at which point they reflect downward at the same angle. Finally, for rays with launch angles between about 10.5° and 11.5°, the spreading between them as a function of range happens at a much greater rate, which reduces the sound intensity in this region (yellow area). A *shadow zone* would exist here were it not for the contribution of rays that have been reflected from the sea surface.

Still, there is a reduced sound intensity near the receiver and this can be quantified with more careful computations of spacing between rays. At the source, a pair of rays launched at $\theta_0 \pm \Delta\theta$ form a *ray tube*, which contains a fraction of the total radiated power, say $\Delta\Pi_A$. The intensity at range r_0 within the space defined by the pair of rays is I_0 and equals $\Delta\ \Pi_A/A_0$, where A_0 is the cross-sectional area of the ray tube. The cross-sectional area in fact will be a strip (Fig. 4) if the source were radiating omnidirectionally. Without loss of generality we proceed on this assumption and compute

$$A_0 = 2\pi r_0^2 \cos\theta_0 \Delta\theta \tag{21}$$

Energy conservation in the context of ray theory states that $\Delta\Pi_A$ must remain constant for the pair of rays over the course of their propagation path (7). The same pair of rays in the vicinity of the receiver assumes a vertical separation Δz. At the receiver the sound speed is c_1, the local grazing

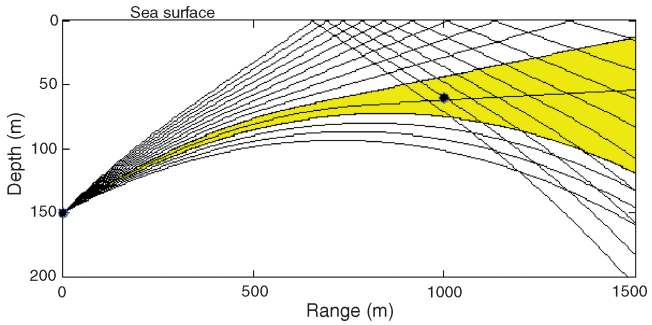

Figure 3. Ray fan corresponding to the sound speed profile of equation 20, with the source at 150 m and the receiver at 60 m and 1000 m downrange. Shown are rays launched from the source with angles between 9° and 16° (every 0.5°). Rays that reach the sea surface will be reflected downward at the same angle; rays with launch angles between about 10.5° and 11.5° spread apart at a greater rate, which reduces the sound intensity in the yellow-colored region.

angle is θ_1, and the cross-sectional area of the ray tube is

$$A_1 = 2\pi r \Delta z \cos\theta_1 \tag{22}$$

where r is the horizontal distance between source and receiver. Since $A_1 I_1$ equals $A_0 I_0$, the transmission loss (TL), defined as 10 log (I_0/I_1), is found to be

$$TL = 10\log\frac{r\Delta z c_1}{r_0^2 \Delta\theta c_0} \tag{23}$$

The direct path is defined by the bundle of rays that propagate directly from source-to-receiver without reflecting or scattering from the sea surface, and the transmission loss for this path, which is within the shadow zone in Fig. 3, is approximately 65 dB. If refraction effects were absent, then the transmission loss for this approximately 1000-m path would be, based on spherical spreading, about 20 log 1000, or 60 dB. The additional 5 dB caused by refraction is a very significant effect in terms of sonar performance.

Our simple example illustrates how ray theory can identify the key propagation characteristics associated with a particular sound speed environment and source/receiver geometry. Numerical propagation codes based on ray theory are used heavily in high-frequency sonar performance evaluations, particularly where computational speed is a critical factor. But, as mentioned, ray theory is an approximation, providing an ever more accurate solution to the wave equation as the frequency increases [thus, ray theory often is called a high-frequency approximation (7, 8)]. Two major deficiencies of ray theory are (1) *caustics*, where the area defined by a pair of rays vanishes (and thus intensity goes to infinity) and (2) *shadow zones*. Our simple approach for computing transmission loss as outlined in equation 23 will become less accurate for field points well inside the shadow zone. Here, more exact solutions to the wave equation are required, and they show that the sound pressure field decays exponentially with perpendicular distance from the shadow boundary, with a decay constant proportional to cubed root of frequency (10).

Notwithstanding the deficiencies caused by caustics, shadow zones, and other effects, ray theory has great intuitive appeal, as illustrated by the ray fan in Fig. 3. Another

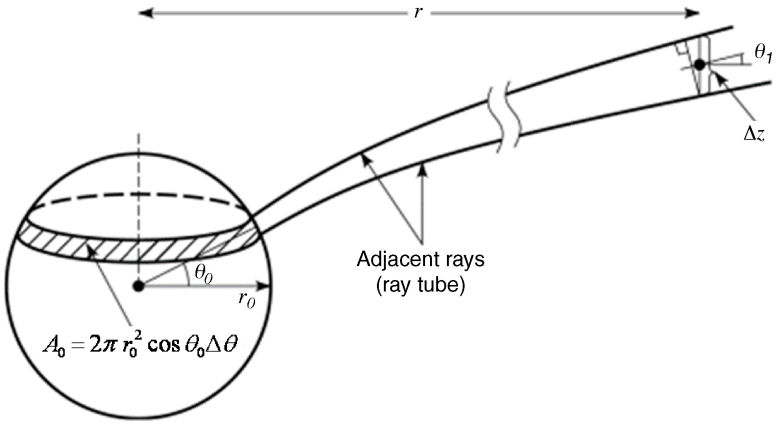

Figure 4. Sketch showing how transmission loss is calculated from the spacing between rays. A sphere of radius $r_0 = 1$ m surrounds the source; and a pair of adjacent rays, initially separated by $\Delta\theta$, form a ray tube that either expands or contracts depending on the sound speed of the intervening medium.

example of the intuition provided by ray theory is a computation of the subset of rays that connect an acoustic source to a receiver; these are called *eigenrays*. Figure 5 shows a set of five eigenrays for a source at depth 25 m, separated by a receiver at range 500 m; these are computed using the sound speed profile shown in Fig. 5a measured in the East China Sea (24). In Fig. 5b, the receiver depth is 25 m, in Fig. 5c, the receiver depth is 52 m, and the eigenrays

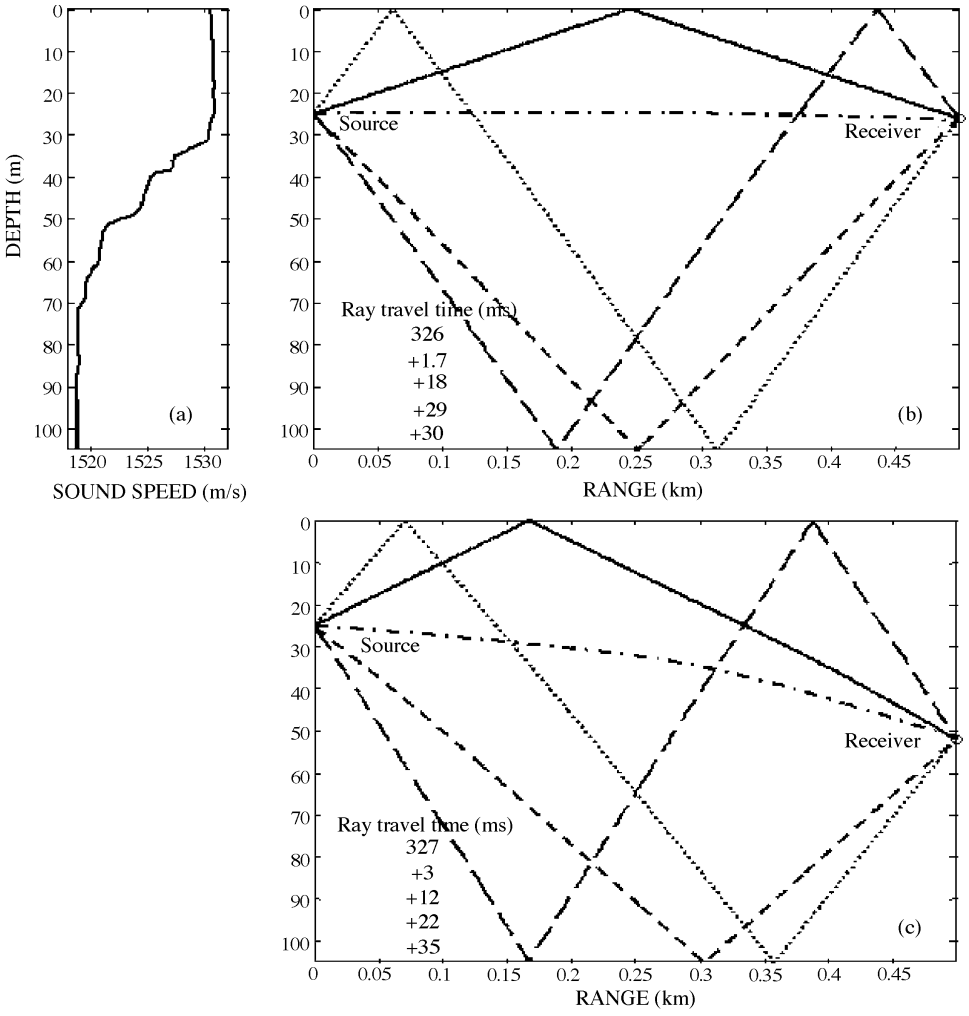

Figure 5. (a) Sound speed profile for site in the East China Sea measured 31 May 2001, 1030 UTC. (b) First five eigenrays based on sound speed profile in (a) between a source at depth 25 m and receiver at depth 25 m, range 500 m. (c) Same as (b) but receiver at depth 52 m. The travel time in ms for the first-arriving eigenray is listed in (b) and (c) with differential travel times for the later arriving eigenrays listed below for each case. (From Reference (24), with permission.)

can be identified by the degree to which they have interacted with the sea surface or seabed, e.g., direct (no interaction), surface, bottom, surface-bottom, or bottom-surface. The direct ray arrives first, with acoustic travel time (in ms) listed in the figure, with differential travel times (in ms) of the later arriving eigenrays listed below each direct ray travel time. The difference in arrival time between the first-arriving direct ray and the last-arriving ray is 30–35 ms, which represents the *time spread* for this channel.

Jensen et al. (8) outline methods to improve ray theory calculations, as well as other, more exact approaches to computing the acoustic field in inhomogeneous media based on wave theory, and Frisk (7) provides a detailed discussion on the relation between solutions derived from ray theory and those derived from the more exact wave theory. Finally, we emphasize that the ocean is neither perfectly horizontally stratified nor frozen in time. Ocean salinity fronts can be crossed, and ocean dynamic processes such as tides and internal waves impart temporal variability. Apel et al. (25) provide telling examples of these effects, placed in the context of a shallow water acoustic propagation experiment, and Flatté et al. (26) provide a comprehensive review on this subject.

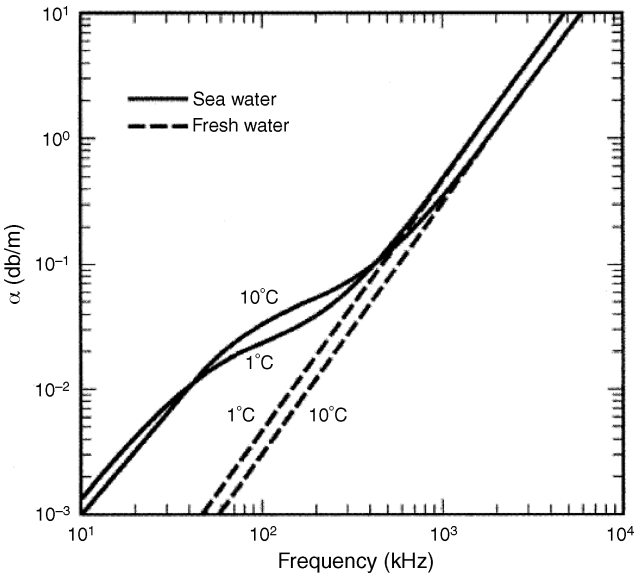

Figure 6. Attenuation rate α (in dB/m) as computed from the François–Garrison empirical formula, at 10 °C and 1 °C. Solid lines are for seawater, and dashed lines are for freshwater. The salinity of seawater is 35 ppt.

SOUND ABSORPTION

As discussed, sound intensity can decay spherically as $\sim 1/r^2$, with r being the range (in meters) from the source; in this case the transmission loss is given by 20 log r in dB re 1 m. Transmission loss in excess of this value is possible as demonstrated in the previous example involving refraction effects as evaluated with ray theory. Transmission loss also can be significantly reduced if, for example, sound is confined to two-dimensional, *cylindrical spreading* within an acoustic channel and the transmission loss is given by 10 log r. Let us collectively refer to such losses as spreading loss, and regardless of the form it takes, we now must add to it an additional loss due to *sound absorption* in water.

Two mechanisms exist for absorption loss. One is a chemical relaxation in response to the passing sound wave (1). In seawater, the presence of both boric acid and magnesium sulfate is largely the cause of this absorption loss. The other is associated with viscosity and affects sound propagation in both seawater and freshwater. Absorption loss usually is expressed by α in dB/m. Francois and Garrison (27) developed a now widely used empirical model for α shown in Fig. 6 for the 10-kHz to 10^4-kHz band. The component of α associated with boric acid is significant only for frequencies $\leq$10 kHz (being hardly noticeable in Fig. 6), whereas the component associated with magnesium sulfate dominates absorption in seawater between roughly 10 kHz and 500 kHz. Beyond about 500 kHz, viscous effects begin to dominate over chemical relaxation effects and α increases with decreasing temperature at the same rate for both fresh- and seawater. Note that the reverse dependence for seawater occurs between about 40 kHz and 400 kHz and that α increases with increasing temperature.

The total transmission loss is the sum of spreading and absorption losses, with the latter (in dB) given by $\alpha\ r$. It is important to notice that once the absorption loss approaches a significant value, it soon will dominate the total transmission loss. For example, when a range is reached such that $\alpha\ r = 10$ dB, then a doubling of this range results in another 10 dB of absorption loss, whereas only a 6-dB additional loss is caused by spherical spreading for each doubling of range. Thus, $\alpha\ r = 10$ dB is a useful guideline to the maximum range for a given frequency; for example, at 10 kHz, $\alpha \approx 1$ dB/km, giving the 10 km mentioned at the beginning of this article as the nominal propagation range for 10 kHz.

REFLECTION FROM BOUNDARIES

Let us return to Fig. 2 and now include differing densities ρ_0 and ρ_1 on each side of the boundary along with the differing sound speeds c_0 and c_1. Let Z_0 equal $\rho_0 c_0/\sin\theta_0$, and let Z_1 equal $\rho_1 c_1/\sin\theta_1$. These variables are *acoustic impedances*, being equal to the ratio of acoustic pressure to particle velocity in the direction normal to the boundary, evaluated at the boundary. The plane wave, or Rayleigh, *reflection coefficient* defined as

$$R(\theta_0) = \frac{Z_1 - Z_0}{Z_1 + Z_0} \tag{24}$$

gives the magnitude and phase of the reflected pressure wave, with the reflected wave having the same grazing angle as the incident wave. The *transmission coefficient* $T = 1 + R$ gives the amplitude and phase of the pressure wave transmitted into the medium characterized by ρ_1 and c_1, with new grazing angle θ_1 (governed by Snell's law). Reflection from the boundary between these two media clearly depends on the ratio between the two characteristic acoustic impedances involved, $\rho_0 c_0$ and $\rho_1 c_1$, but also on the grazing angle as contained in Z_0 and Z_1.

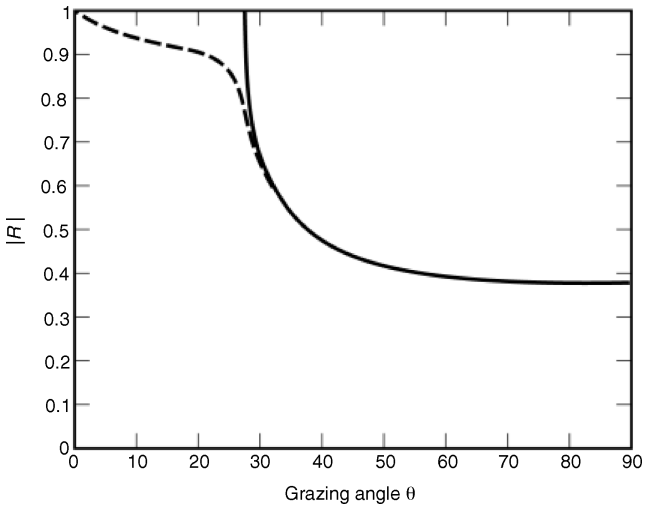

Figure 7. Magnitude of the reflection coefficient $|R|$ versus grazing angle θ_0 defined relative to the horizontal. The solid line is for $\delta = 0$, and the dashed line is for $\delta = 0.0116$.

The air–sea interface represents a boundary where the characteristic acoustic impedance goes from its seawater value of about 1.54×10^6 kg m^{-2} s^{-1}, or 1.54×10^6 rayls (the standard MKS unit for characteristic impedance is a *rayl* equal to 1 kg m^{-2} s^{-1}), to the substantially lesser value in air of about 430 rayls, based on a sound speed in air of 331 m/s and a density of 1.29 kg/m^3. For such an extremely high contrast in characteristic impedance, it is easy to show that $R \approx -1$, or $|R| \approx 1$, and that the phase of R is π. The transmission coefficient $T \approx 0$, and a negligible amount of sound is transmitted from water into the air. It usually is assumed in acoustic modeling that R for the air–sea interface is precisely -1.

Reflection from the seabed is more varied and interesting. The ratio of seabed sediment to seawater characteristic impedance can range from nearly unity for muddy-type seabeds to $\sim$10 for extremely hard, rocky seabeds. Now let $\rho_0 c_0$ and $\rho_1 c_1$ represent seawater and seabed media, respectively. Figure 7 shows the reflection coefficient modulus $|R|$ for a seabed characterized by $\rho_1/\rho_0 = 1.97$ and $c_1/c_0 = 1.126$, representing seabed sediments off Panama City, Florida (28). Absorptive losses in the seabed also typically will be high relative to that of seawater alone; and δ, known as the loss tangent (29, 30), includes this effect by making the sound speed in the seabed complex; i.e., c_1 goes to $c_1/(1 + i\,\delta)$. The solid line is computed with δ set to zero, and the dashed line is computed with $\delta = 0.0166$ (28), which is equivalent to about 20-dB/m attenuation in the sediment when the frequency is 40 kHz.

For the case of $\delta = 0$, $|R| = 1$ for all grazing angles less than about 27.36°. For this range of incident grazing angles, the seabed reflects all the energy back into the seawater medium (total internal reflection occurs). At exactly $\theta_c = 27.36°$, known as the *critical angle*, a transmitted wave propagates into the seabed sediment, thereby reducing the amplitude of R. The critical angle is given by Snell's law:

$$\theta_c = \cos^{-1}(c_0/c_1) \tag{25}$$

defining the point at which θ_1 transitions from an imaginary to a real angle. Flow of acoustic energy into the seabed only can occur when θ_1 contains a real component; when θ_1 is purely imaginary, the acoustic field in the seabed is evanescent and cannot transport energy (7). The critical angle is one of the most important acoustic parameters of the seabed; the higher the ratio of c_1/c_0, the higher the critical angle. When a nonzero δ is used, the results are modified slightly, and the complex sound speed in the seabed makes θ_1 complex for all incident grazing angles θ_0. Thus, a small amount of energy is lost into the seabed even for $\theta_0 \ll \theta_c$, as shown by the dashed line.

Bottom reflection loss (7) is defined as $-20 \log |R|$ and is a measure of the energy lost by sound propagating into the seabed. When $|R| = 1$, the loss is 0 dB, and all the energy is trapped in the upper water layer. For the example shown in Fig. 7, the loss increases to about 8.5 dB for grazing angles greater than θ_c; and "bottom bounce" ray paths, which are common in a shallow water environment (as shown in Fig. 5), are attenuated substantially if their grazing angles exceed θ_c (31). Note that in most seabeds, the picture will be more complicated than that depicted in Fig 7. For example, if there are sediments layers with thickness on the order of an acoustic wavelength, bottom reflection loss will be a function of frequency. An example is Fig. 8 showing measurements of bottom reflection loss made in the East China Sea (24) as a function grazing angle and frequency. The measurements are compared with a model for reflection loss based on a sediment layer that overlays a homogeneous sediment half-space.

REVERBERATION AND SCATTERING PHENOMENA

Consider a plane wave incident on a small bubble having radius a with $ka \ll 1$; the bubble will *scatter* a fraction of the incident plane wave sound energy into a continuous distribution of scattering angles. We contrast this process with that of reflection from a smooth planar boundary discussed in the previous section; in that case, there was only one reflected angle equal to the direction of specular reflection (not including the refracted wave that penetrates the boundary). Generally, specular reflection predominates if the object being ensonified has a local radius of curvature that is large compared with the wavelength of the incident sound field (as in the case for a planar-like boundary). Sound scattering can occur whenever sound waves traverse a region of inhomogeneities in the medium, such as a region of suspended scatterers consisting of particulate matter, biota in the form of zooplankton or fish, or bubbles. The inhomogeneities also may take the form of fluctuations in the physical properties of water such as its temperature or salinity, or fluctuations in fluid velocity associated with patches of turbulence.

Volume Reverberation

Volume reverberation is the term used to describe scattering from the total volume of water ensonified by an incident sound field. The scattering from entities entrained in the water provides one basis for remote sensing of water column properties using high-frequency underwater sound.

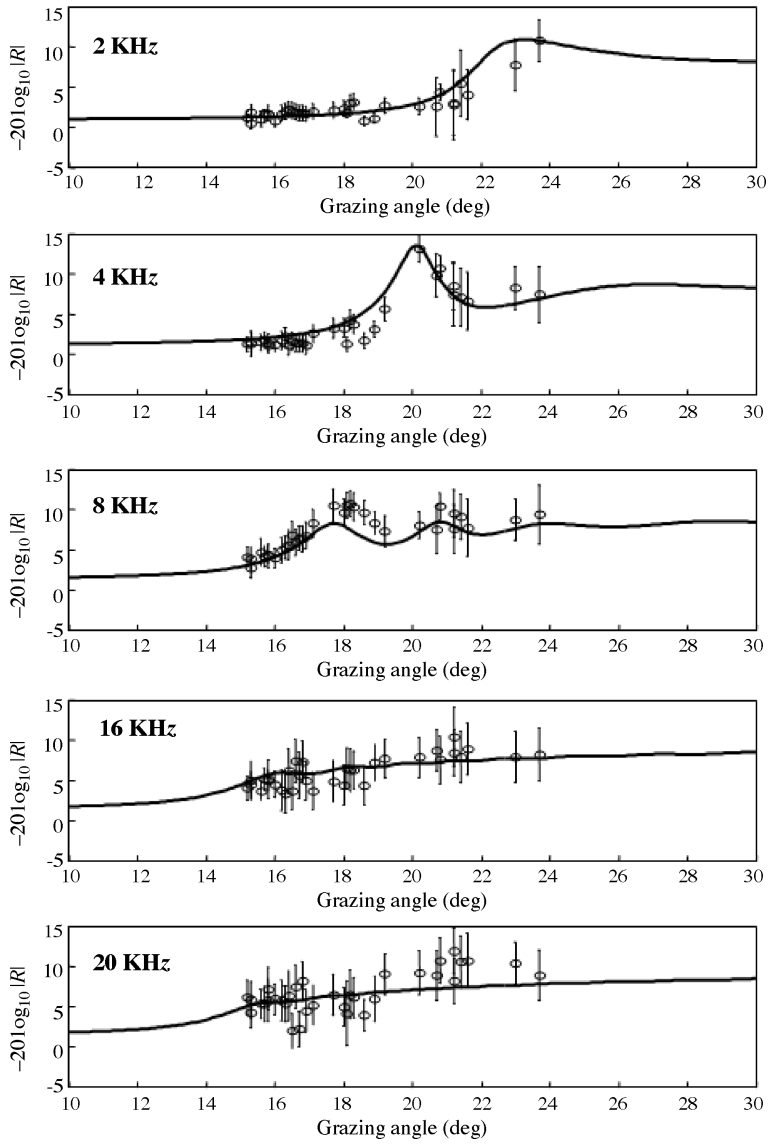

Figure 8. Measured bottom reflection loss as a function of grazing angle and frequency compared with a model for $-20\ \log|R|$ based on sediment layering overlaying a homogeneous half-space. (From Reference (24), with permission.)

Similarly, there can be either seafloor or sea surface reverberation, each of which pertains to the scattering contribution from the total area of ensonified sea surface or seafloor. Total reverberation is the incoherent sum of the volume and area contributions. For a source and receiver that are colocated, such as a typical transducer configuration for remote sensing applications, the reverberation is *monostatic*; and if source and receiver locations differ, the reverberation is *bistatic*.

To understand volume reverberation, we continue with the example of a small bubble with $ka \ll 1$. The bubble in fact scatters sound equally in all directions, or isotropically, and the total sound power Π_s intercepted and scattered is given by

$$\Pi_s = I_{\text{inc}}\sigma_s \tag{26}$$

where I_{inc} is the sound intensity incident on the bubble and σ_s is the bubble's total scattering cross section in m^2. Note that Π_s is the solid angle integral of $\Pi(\theta, \phi)$, where the latter represents the sound power scattered in directions $[\theta, \phi]$ away from the bubble. For isotropic scattering, $\Pi(\theta, \phi)$ is the same in all directions, say $\Delta\Pi$, in units of power per steradian and Π_s is $4\ \pi\ \Delta\Pi$. For the monostatic case, the quantity actually measured is the backscattered intensity from the bubble I_{bs}, which is given by

$$I_{bs} = \frac{\Pi_s}{4\pi r^2} = \frac{I_{\text{inc}}}{r^2}\frac{\sigma_s}{4\pi} \tag{27}$$

For a bubble, or any other isotropic scatterer, we can write $\sigma_{bs} = \sigma_s/4\pi$, where σ_{bs} is the bubble's *backscattering cross section*. This is the power per unit intensity per steradian scattered in the direction toward the transducer (i.e., back toward the source of the incident sound). For an arbitrary scatterer, such as a zooplankton, which does not scatter isotropically, σ_{bs} thus is defined by its relation to I_{bs} using

$$I_{bs} = \frac{I_{\text{inc}}}{r^2}\sigma_{bs} \tag{28}$$

In remote sensing measurements, often there is need to compare relative levels of scattering, say between bubbles

and zooplankton. Therefore, if the measurements represent backscattering, then it is best to report σ_{bs}. If the scatterer is known to scatter isotropically, then one can report $\sigma_s = 4\pi\ \sigma_{bs}$ if need be. The target strength (3) *TS* is the decibel equivalent of σ_{bs}, i.e., equal to 10 log σ_{bs} in dB re 1 m^2. Note that whenever target strength is evaluated, then σ_{bs} must be used and expressed in m^2.

Now consider a cloud of scatterers at range r corresponding to the cloud's center. An elemental volume dV produces a backscattered intensity dI_{bs} at the receiver given by

$$dI_{bs} = \frac{I_{\text{inc}}}{r^2} s_V dV \tag{29}$$

The quantity $s_V dV$ assumes the role of σ_{bs} for an assemblage of scatters within a volume dV, where s_V is the backscattering cross section per unit cubic meter of water with dimension m^{-1} (and, like σ_{bs}, also must be considered as "per steradian"). The *scattering strength* S_V is 10 log s_V in dB re 1 m^{-1}. Sometimes the symbol m_V is used, with the meaning $m_V dV$ being total sound power scattered into all directions by volume dV. Analogous to the foregoing remarks on σ_{bs}, if it can be assumed that scattering is isotropic, then one can write $m_V = 4\pi s_V$.

The total backscattered intensity results from summing all dV, some of which are away from the acoustic axis. For these contributions, the incident and backscattered intensity need to be compensated for the effects of the beam pattern $b(\theta, \phi)$. The results leads to the concept of an effective volume, or reverberation volume (3), based on integration of the two-way intensity pattern $b2(\theta, \phi)$. If ψ is defined as the integral of $b^2(\theta, \phi)$ over all directions θ and ϕ, then the effective volume at range r for a pulse of length τ, is $\psi\ (c\ \tau/2)\ r^2$, and the total backscattered intensity is

$$I_{bs} = \frac{I_0 r_0^2}{r^4} s_V \frac{c\tau}{2} r^2 \Psi \tag{30}$$

where the incident intensity is referenced back to I_0 via spherical spreading with $I_{\text{inc}} = I_0(r_0/r)^2$.

Upon adding attenuation, equation 30 can be recast into the *sonar equation* that expresses this concept in decibels,

$$RL = SL - 40\log r - 2\alpha r + S_V + 10\log\frac{c\tau}{2} r^2 \Psi \tag{31}$$

where the *reverberation level*, RL, is 10 log I_{bs} and the effect of two-way absorption loss is now included as $2\alpha\ r$. (Since $r_0 = 1$ m, the reference term 10 log $r^2{}_0$ usually is ignored.) Urick (3) also provides useful approximations to ψ for standard transducer shapes. Continuing with the example of circular piston transducer of diameter d, $\psi \approx 1.87(\lambda^2/\pi\ d2)$, which is a factor of about 2 less than the same integral over the one-way pattern as in equation 13. This result is expected because the equivalent two-way beam necessarily must be narrower than its one-way counterpart.

Scattering from Bubbles. Bubbles must be recognized for their particularly important role in high-frequency underwater sound. They are sources of scattering and attenuation (32–38), can produce changes in the speed of sound of sound (39–41), and are contributors to ambient underwater noise (42–44). Such effects are most evident in the vicinity of the sea surface, where bubble concentration is highest, and their numbers continually are replenished by the action of surface breaking waves. Medwin and Clay (1) summarize a portion of recent experimental work on ambient ocean bubble populations, which suggests that most bubbles near the sea surface have radii within the range 10 μm to 1000 μm. To be sure, larger bubbles exist, but their increased buoyancy would bring them quickly to the surface. At 30 kHz, the acoustic wavenumber $k \approx 125\ m^{-1}$, and thus, $ka \ll 1$ over this entire range of bubble radii. In the $ka \ll 1$ regime, the incident sound field essentially is uniform over the bubble's surface, and there will be a large monopole resonance response by the bubble to an incident sound field if the sound frequency matches the bubble's resonant frequency. The backscattering cross section for a bubble in the $ka \ll 1$ regime is given by

$$\sigma_{bs} = \frac{a^2}{[(f_R/\ f)^2 - 1]^2 + \delta^2} \tag{32}$$

where in this equation δ represents a damping coefficient associated with thermal and viscous damping effects, and all units are in MKS (1, 3). Scattering is maximal at frequency f equal to the resonant frequency f_R for a bubble radius a_R, as given by approximately

$$a_R = \frac{3.25\sqrt{1 + 0.1z}}{f_R} \tag{33}$$

where z is the depth.

Recall from the previous discussion that since bubbles scatter isotropically, $\sigma_s = 4\pi\ \sigma_{bs}$. In backscattering measurements, the influence of a single bubble's total scattering cross section σ_s is to incrementally weaken the incident, interrogating sound beam caused by the power scattered isotropically by the bubble. An absorption cross section σ_a similarly quantifies this incremental weakening of the incident sound beam from a single bubble caused by the thermal and viscous damping effects (15). The sum $\sigma_s + \sigma_a$ gives the extinction cross section σ_e that combines the effects of absorption and scattering, and it can be shown that $\sigma_e = \sigma_s\ (\delta/ka)$. A compensation for this effect, called bubble-mediated attenuation (38), often is necessary in the interpretation of field measurements.

Figure 9 shows the target strength of a bubble versus bubble radius a for bubbles near the sea surface, when they are ensonified by frequencies of 30 kHz, 60 kHz, and 120 kHz. Taking 30 kHz, the maximum resonant response is produced by a bubble with a radius of 109 μm. It is interesting to compare σ_{bs} for a rigid sphere of the same radius when it also is ensonified at 30 kHz. Provided $ka \ll 1$, then σ_{bs} for a rigid sphere is

$$\sigma_{bs} = \frac{25}{36} a^2 (ka)^4 \tag{34}$$

that goes as $(ka)^4$, characteristic of Rayleigh scattering (1). For the rigid sphere, $\sigma_{bs} = 1.6 \times 10^{-16}$ compared with $\sigma_{bs} = 1.9 \times 10^{-6}$ for the same-sized bubble. Such a huge scattering advantage for bubbles when ensonified at their resonance frequency is the basis for using multifrequency acoustical backscattering techniques to sense remotely oceanic bubbles (35,37,45).

Acoustic backscattering from a cloud of bubbles also is interpreted in terms of s_V, which is defined in this case as

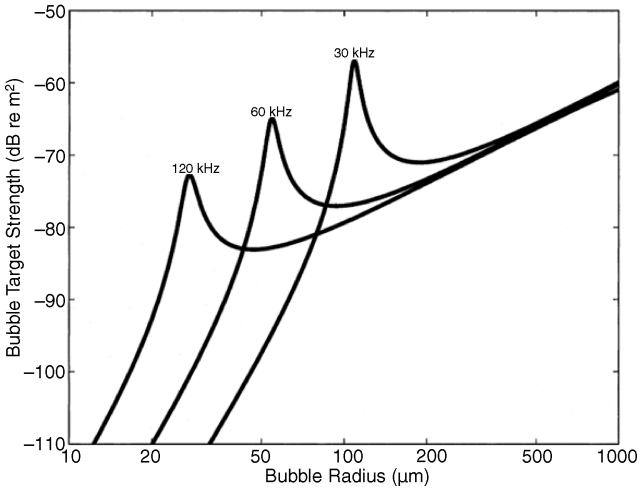

Figure 9. The target strength $10 \log \sigma_{bs}$ of a bubble versus bubble radius a when ensonified by 30 kHz, 60 kHz, and 120 kHz.

the integral over bubbles of many sizes:

$$s_V = \int \sigma_{bs}(a) N(a) da \tag{35}$$

where $N(a)$ is the bubble size distribution giving the number of bubbles per unit volume per unit radius, with radii between a and $a + da$.

For inverting and interpreting acoustic backscattering data from bubbles, an accounting also must be made for the added loss in intensity associated with propagating distance dr into the interior of a bubble cloud. The result is a bubble attenuation coefficient α_b (in dB/m) given by (1)

$$\alpha_b = 4.34 \int \sigma_e(a) N(a) da \tag{36}$$

The combined effects of scattering and absorption from bubbles can have an enormous impact on sound propagation. Recent measurements (46) made within a coastal surf zone region show that α_b can often exceed 4 dB/m at frequencies near 60 kHz (compare this with 60-kHz absorption in seawater of about 0.02 dB/m). Whenever such high α_b are in effect, the water essentially is opaque to acoustic transmission.

Bubbles also can influence the sound speed in addition to their scattering and absorption effects. The result is a frequency-dependent change in sound speed, $\Delta c(f) = c_0 - c_b(f)$, where in this case c_0 and $c_b(f)$ are the speed of sound in bubble-free water and bubbly water, respectively. Lamarre and Melville (47) measured $\Delta c(f)$ near the ocean surface at a wind speed of about 8 m/s. Their results show $\Delta c(f)$ can reach about 20 m/s for frequencies between 10 and 20 kHz, whereas for higher frequencies, $\Delta c(f)$ decreases, going slightly negative to about −5 m/s for their highest frequency of 40 kHz. Ultimately, $\Delta c(f)$ approaches zero as the ensonification frequency is increased well beyond the resonant frequencies associated with the population of bubbles. It is for this reason that acoustic devices for measuring the speed of sound underwater operate in the MHz frequency range and are insensitive to the effects of bubbles on sound speed (1).

Scattering from Fish and Zooplankton. Underwater acoustic surveys using high-frequency sound have been used to assess and manage fisheries and zooplankton stocks since the 1960s (48). In rivers of Alaska (49) and western Canada (50), sonars operating in the 100-kHz to 500-kHz range are used to count migratory salmon. Counting individual echoes from salmon is the basis for enumeration, and the sonar beams usually are oriented perpendicular to the river flow (side-scan) and approximately parallel to the river bottom. Trevorrow (50) discusses the issues in recognizing fish echoes from background reverberation characteristic of the riverine environment.

For more dense aggregations as found in pelagic stocks of fish and zooplankton, measurements of s_V are converted (51) to biomass in kg/m^3, or animals per m^3. For an acoustically homogeneous population of marine life with density N (number per m^3), each having the same σ_{bs}, then, according to single scattering theory (52), the observed s_V will equal $N\sigma_{bs}$. For an acoustically heterogeneous population with differing σ_{bs}, for example N^i characterized by σ^i_{bs}, the relation becomes $s_V = \Sigma N^i \sigma^i_{bs}$.

Thus, it is clear that accurate estimates of single fish or zooplankton target strength are essential for obtaining quantitative estimates of animal abundance. As is the case with bubbles, schools of fish also can attenuate the sound. Masahiko et al. (53) measured the attenuation of sound by schooling fish at frequencies between 25 kHz and 200 kHz, for typical fish school densities encountered in field observations. Their results, however, suggest that sound attenuation by schooling fish would have a negligible effect on abundance estimates. (This is not the case at frequencies less than 10 kHz, as here a resonance associated with the swimbladders of fish can produce significant attenuation).

The sound scattering properties of a single fish at high frequencies still depends in large part on whether the fish has a swimbladder. Foote (54) demonstrated experimentally that the swimbladder contribution to σ_{bs} is approximately 90% for some combinations of fish size and acoustic frequency. For example, at 38 kHz, the target strength for a 30–35 cm length cod (swimbladdered) is about −30 dB. The target strength for a similar-sized mackerel (non-swimbladdered) is about −40 dB. The large difference is not from a resonance effect; instead, it is from the large acoustic impedance contrast between water and the air-filled swimbladder.

Fish orientation, or aspect, also is an important factor. For surveys of pelagic fish stocks, measurements of the *dorsal aspect* target strength are needed to quantify the data. For counting migratory salmon in rivers using side-scan sonars, the *side aspect* target strength is of interest. Dahl and Mathisen (55) studied target strength variability from aspect by rotating a fish in the yaw plane while making backscattering measurements. The side aspect target strength of a 50-cm-length salmon at 420 kHz is about −25 dB, and when the fish was rotated to be head-on the target strength fell to about −45 dB, or scattering was reduced by a factor of 100.

For zooplankton, target strength depends in large part on ka_{sr}, where a_{sr} is the animal's equivalent spherical radius equal to about 20% of its total length (51, 56). For $ka_s \ll 1$, Rayleigh scattering predominates; and therefore

for a given-sized animal, σ_{bs} goes as acoustic frequency to the fourth power. The optimum frequency for zooplankton studies, thus, clearly represents a balance between stronger scattering afforded by higher frequency and the effects of increasing absorption with frequency. Frequencies equivalent to $ka_{sr} = 0.8$ to 1.8 are suggested by Holliday and Pieper (51). Stanton *et al.* (57) developed a ray theory solution to the problem of sound scattering by a deformed fluid cylinder, which serves as a model for zooplankton. This work was extended (58) to handle the case of random orientation of zooplankton with respect to the sonar beam, and formulas for σ_{bs} compare favorably with measurements made over the ka_{sr} range 0.25 to 7.50.

The Doppler shift of the backscattered signal provides the component of the scatterer's velocity parallel to the sonar beam, which is estimated at different ranges along the sonar beam with a range resolution of $\Delta r \approx c\tau/2$. If it can be assumed that the scatterers are passive tracers of the fluid velocity, then such estimates represent the actual water velocity. These scattering-based estimates of velocity are weighted by the σ_{bs} of the individual scatterers within the sonar beam (59), and on occasion, they can be contaminated by the passage of stronger-scattering and actively moving fish targets. Pinkel (60) reviews Doppler sonar backscattering methods used in the study of internal wave fields, for which zooplankton are the primary source of backscatter. Plueddemann and Pinkel (61) also used Doppler sonar to study the daily migration pattern of zooplankton within the mesopelagic zone (100 m to 1000 m). Vertical migration of a sound scattering layer of zooplankton was observed moving toward shallower depths around sunset and toward deeper depths around sunrise, with Doppler shifts indicating a migration rate between 1 cm/s and 4 cm/s. Smith (22) discusses Doppler sonar in the context of studying near-surface dynamics, for which bubbles are the primary source of scatter and, therefore, tracers of velocity.

Scattering from Turbulent Microstructure. Fluctuations in the physical properties of water may produce significant scattering if the spatial scale of these fluctuations is similar to the acoustic wavelength. In particular, fluctuations in the *index of refraction* $\eta(\boldsymbol{x}) = c_0/c(\boldsymbol{x})$ are related to s_V via (62, 63)

$$s_V = 2\pi k^4 \Phi_\eta(\kappa_B) \tag{37}$$

where $\Phi_{\eta(\kappa_B)}$ is the three-dimensional wavenumber spectrum of η evaluated at its Bragg wavenumber κ_B, which for backscattering reduces to two times the acoustic wavenumber k (63). For 100 kHz, fluctuation scales in η that are of order 1 cm are responsible for scattering; such scales are classified loosely as *microstructure*. An important issue concerns the potential ambiguities in remote sensing of zooplankton in the presence of strong turbulent fields. This was examined experimentally by Stanton *et al.* (64), who concluded that when zooplankton and strong turbulent fields are colocated, their separate scattering contributions can be of similar magnitude. They suggest discrimination between these two scattering mechanisms is possible through spectral analysis of echoes using broadband sonars.

Acoustic Images of Volume Reverberation

In this section we present three examples of acoustic remote sensing of water column properties, illustrating scattering from bubbles, zooplankton, and turbulent microstructure. The examples are from separate ocean experiments, all of which used vertically oriented sonars operating at high frequency. Such measurements have the distinct advantage of being both noninvasive and capable of giving an unaliased picture of both biological and physical oceanographic processes.

Figure 10 is an image of S_V made with a 240-kHz uplooking sonar. The data are from an experiment conducted from the research platform *Flip*, which was designed to study the evolution of bubble clouds produced by breaking waves (37). The measurements were made with a sonar mounted on the end of a subsurface boom, attached to *Flip's* hull 28.5 m below the water line. With this configuration, the sonar had an unobstructed view looking up toward the surface, whereas *Flip* served as a very stable platform and was subjected to minimal heave motion. The wind speed is 10 m/s, and the peak period of ocean swell is 14 s. The time origin for this 2-minute display of S_V is established by an abrupt increase in background noise. This noise, called a noise emission, and the increased scattering to the right of time origin are both postulated to originate from a breaking wave observed directly above the sonar with a video camera.

Figure 11 is an echogram from Mathisen and Macaulay (65) showing a dense aggregation of Antarctic krill (*Euphausia superba*). The measurements were made during the austral summer near Elephant Island in the Weddell Sea, using a 120-kHz downlooking sonar towed behind a ship at a depth of 10 m. The horizontal axis in this case represents range, and based on the ship's speed of 11 km/h, the 40 minutes of data shown here cover a 7.3-km transect. The seabed is shown on the lower left-hand side initially at a depth of 180 m, with depth slowly decreasing over the course of the transect. The data represent a synoptic visualization of an enormous biomass of Antarctic krill. Upon remaining congregated continuously for days, as was in the case shown here, the congregation is known as super swarm.

The third example (Fig. 12) is from Pinkel *et al.* (66) and shows the passage of internal solitary waves (solitons) as recorded by a 167-kHz downlooking sonar in the western equatorial Pacific. The soliton wave packet consists of three downward pointing crests, the first approximately 60 m in amplitude with reduced amplitudes for the second and third crests. The backscattered intensity (proportional to S_V) increases during the passage of each crest, while decreasing slightly between crests. The authors have calculated flow streamlines (for which the tangent is parallel to the flow) shown as superscribed black lines. Upon passage of the third crest, the high scattering levels persist for approximately 4 hours. The authors postulate that Bragg scattering from turbulent microstructure associated with the passage of the solitons is responsible for the enhanced scattering. The 167-kHz frequency thus implies that fluctuation scales of about 0.5 cm are responsible for the scattering.

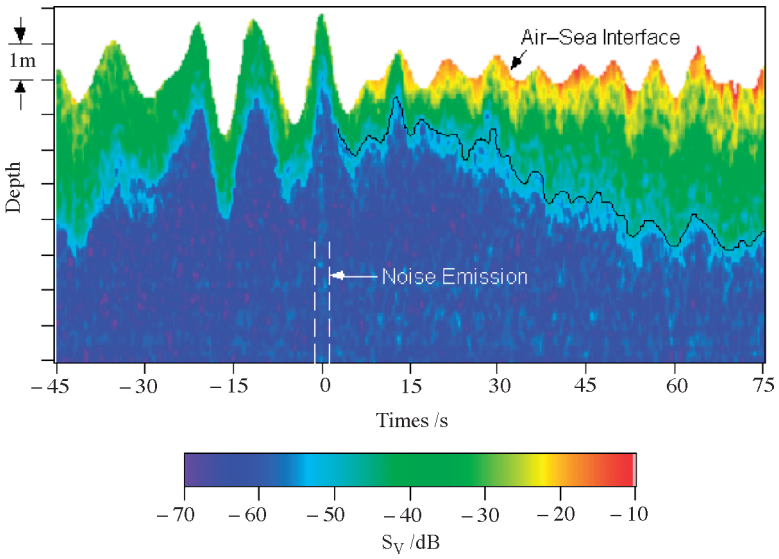

Figure 10. Acoustic volumetric backscattering from near the surface of the ocean (expressed in decibels as S_V) made with a 240-kHz uplooking sonar, 2 minutes of data shown. The noise emission that defines the time origin is shown as a faint vertical streak between the dashed white lines. The time origin denotes the start of a breaking wave event occurring directly above the sonar as confirmed with video analysis. The black line to the right of $t = 0$ follows the $S_V = -50$ dB contour. (From Reference (37) with permission.)

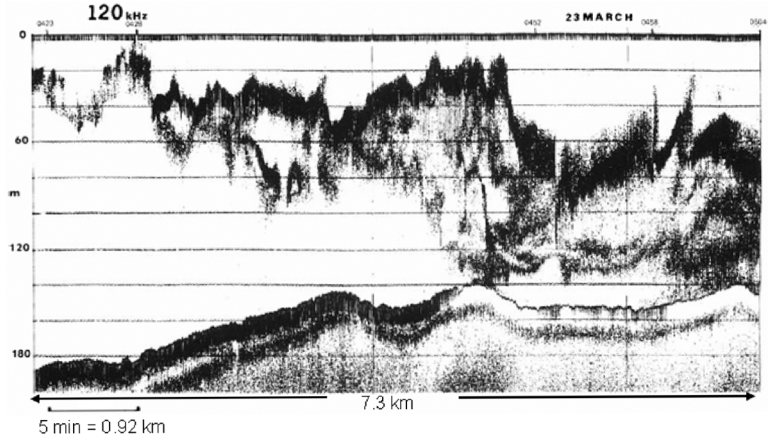

Figure 11. Echogram of super swarm of Antarctic krill, made with 120-kHz downlooking sonar on March 23, 1981 from 0423 to 0504 (GMT) near Elephant Island. The echogram pixel density is proportional to S_V. The horizontal axis is range, with total range of transect equal to 7.3 km based on total time (40 minutes) and speed of ship (11 km/h). The bottom is observed on the left-hand side beginning at 180 m, with depth slowly decreasing over the course of the transect. (From Reference (65), with permission.)

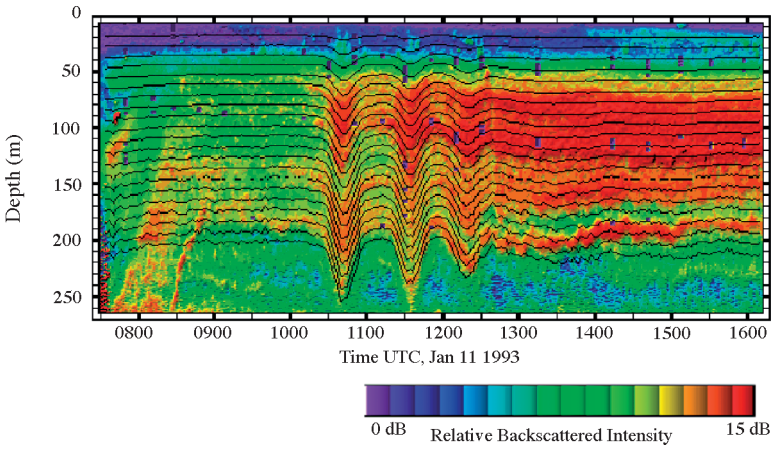

Figure 12. Acoustic scattering in the form of relative backscattered intensity (proportional to S_V) as recorded by a 167-kHz downlooking sonar in the western equatorial Pacific, showing the passage of internal solitary waves. Calculated flow streamlines are shown as superscribed black lines. Squares indicate regions of the water column with unstable density gradient. (From Reference (66), with permission.)

Sea Surface and Seabed Reverberation

A contribution to reverberation level associated with scattering from the sea surface, seafloor, or both, can often be identified. This contribution is $S_S + 10 \log A$, where S_S is the *surface* or *seabed scattering strength* and A is the effective area of sea surface or seabed that is the source of backscattering. Whenever surface scattering is operative, $S_S + 10 \log A$ would be added to the right side of equation 31. Here $S_S = 10 \log\sigma$, where σ is the backscattering

cross section per unit area of sea surface or seabed (3) and thus a dimensionless quantity (unlike the σ_{bs} that applies to the scattering by discrete underwater objects or marine life).

The effective scattering area A depends on the grazing angle θ with respect to the scattering surface, sonar pulse length τ, range r, and the sonar beam pattern. Two simple examples are given using the conical beam pattern from a circular piston transducer in equation 10. First, the effective area can be pulse length-limited; in which case, it is given approximately as $A_\tau = (c\,\tau/2)r\,\Phi$, where Φ is the angle in radians between the -3 dB points of $b(\theta)$ given in degrees by equation 11. Second, the effective area can be independent of pulse length and instead beam-limited; in which case, it is given approximately as $A_b \approx (\pi/4)\Phi^2 r^2/\sin(\theta)$. The effective scattering area is the lesser of A_τ and A_b. Careful estimates of the effective scattering area are critical to recovering reliable estimates of S_S from field data. Jackson *et al.* (67) summarize an accurate approach to estimating scattering area that accounts for practical realities such as non-conical beams and seafloor slope, and Dahl et al. (68) discuss issues pertaining to beam-limiting versus pulse length-limiting estimates of the scattering area.

Volume scattering from the water column clearly affords many opportunities to invert ultrasonic measurements of S_V to gain information about the water column. With surface scattering, on the other hand, greater emphasis is placed on modeling S_S to determine its effect on the performance of sonar systems. Note that for high frequencies greater than about 10 kHz, bubbles residing just beneath the sea surface are in fact the major source of sea surface reverberation (68). Variability of high-frequency acoustic backscatter from the region near the sea surface was studied by Dahl and Plant (69), who developed a model probability density function for S_S. Their study also suggested a link between acoustic variability and the passage of bubble clouds advecting through an ensonified region close to the sea surface.

Jackson *et al.* (28) present a model for high-frequency backscattering from the seabed and its comparison with data. The bottom reflection coefficient, as in equation 24, is an essential part to any model for predicting backscattering from the seabed, and the influence of the critical angle in equation 25 is often observed in measurements. In addition to sonar performance evaluation, physically based models for bottom scattering now are being used in the bottom classification problem, for which acoustic scattering data from the seabed are inverted to estimate seabed properties (70) or to relate temporal changes in bottom scattering to benthic changes (71).

ACOUSTIC IMAGING

We conclude this article on high-frequency underwater sound with a brief introduction to *acoustic imaging*. Figures 10–12 give an interesting visual display and provide valuable quantitative information on water column properties. But they are not both truly two-dimensional (or three-dimensional) and relatively instantaneous. (Figure 11 has true two-dimensional features, but it was gathered over a 40-minute period.)

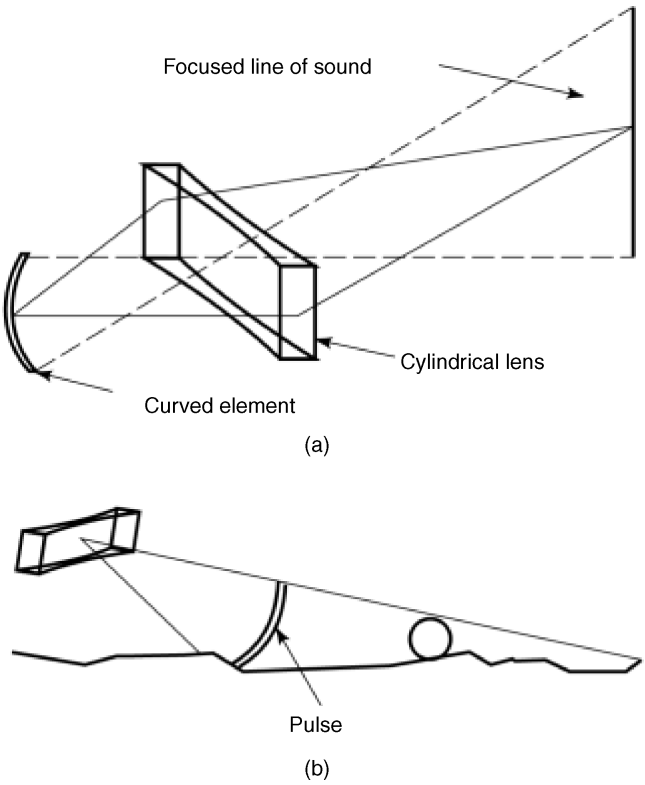

Figure 13. Illustration of a line-focus system. (a) A focused line of sound is made by the combination of cylindrical lens and curved transducer element. The lens forms the azimuthal pattern (solid lines), and the curved element forms the elevation pattern (dashed lines). (b) A pulse from a line-focus system generates a series of echoes returning from the ensonified line on the bottom. (From Reference (72), with permission.)

Underwater acoustic imaging systems that use acoustic lenses and operate at frequencies in the MHz range can produce truly two-dimensional images in near real-time. Like an optical lens, an acoustic lens refracts and focuses sound to within a limited space. The primary function of an acoustic lens is to move the far field closer to the transducer, as well as to provide additional focusing gain (16). The *object plane* refers to the surface to be imaged, and the *image plane* refers to the surface upon which the image is formed (such as the retina of our eye). An example of an acoustic lens is illustrated in Fig. 13, which shows a line-focus system that maps a line in the object plane to a line on the image plane (72). In practice, the object plane is slanted with respect to the beam axis, and the acoustic imaging system thus interrogates the object plane along the line as a function of time as in Fig. 13b.

An example of a lens-based acoustic imaging system is the dual-frequency identification sonar or DIDSON (73) that gives near-video-quality images in turbid and dark water. The standard DIDSON operates at 1.8 MHz and 1.1 MHz, with beam resolutions of 0.3° and 0.6°, respectively, and provides images of objects from 1 m to over 30 m in range. A longer range DIDSON operates at 1.2 MHz

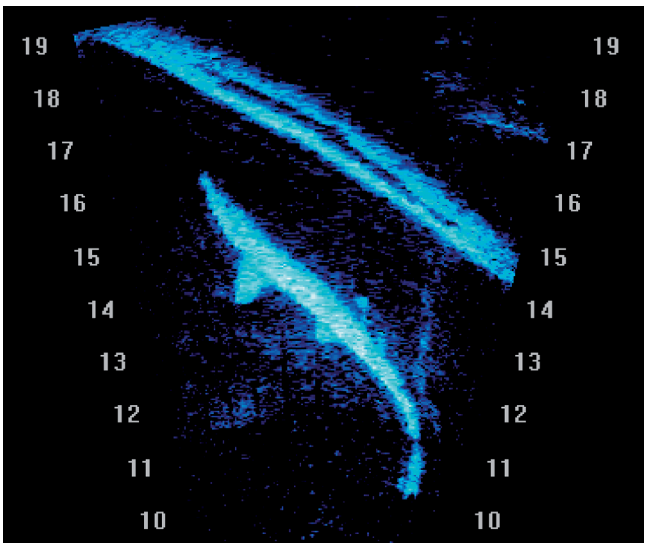

Figure 14. Single frame from a DIDSON video showing a shark (length 2.4 m) in Oceanopolis, an aquarium in Brest, France. The data were collected with a Diver Held DIDSON, and the numbers indicate the range in m of the shark from the DIDSON. (Image provided to author by Sound Metrics Corp. and was obtained by Jean-Yves Cueff, NEOTEK.)

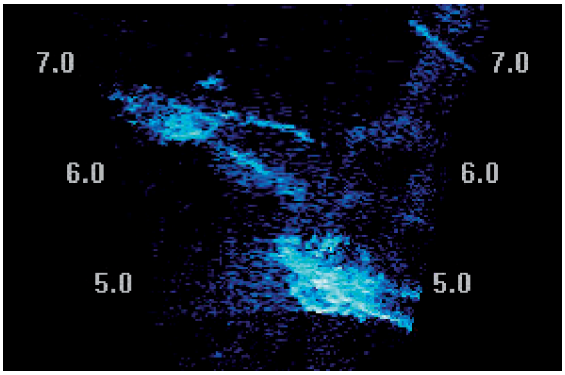

Figure 15. Single frame from a DIDSON video showing two SCUBA divers in Lake Union, Seattle. Numbers indicate the range in m of the divers from the DIDSON. (Image provided to author by Sound Metrics Corp.)

and 0.7 MHz, with beam resolutions of 0.6° and 0.8°, respectively, and can image objects out to 80 m.

Two example images from the DIDSON (each representing a single frame from a video record) are shown in Figs. 14 and 15. The image of a 2.4-m-length shark taken in an aquarium in France by a diver-held DIDSON (Fig. 14) illustrates how such imaging can be used for marine species identification, and the image of two divers in Lake Union, Seattle (Fig. 15), illustrates how such technology can be applied to surveillance.

BIBLIOGRAPHY

1. H. Medwin and C. S. Clay, *Fundamentals of Acoustical Oceanography*, San Diego, CA: Academic Press, 1998.
2. R. C. Spindel, Oceanographic and navigational instruments, in M. C. Crocker (ed.), *Encyclopedia of Acoustics*, Vol. I, New York: Wiley, 1997, pp. 581–589.
3. R. J. Urick, *Principles of Underwater Sound*, New York: McGraw-Hill, 1983.
4. D. R. Jackson and M. D. Richardson, *High-Frequency Seafloor Acoustics*, New York: Springer, 2007.
5. J. A. Catipovic, Acoustic telemetry, in M. C. Crocker (ed.), *Encyclopedia of Acoustics*, Vol. I, New York: Wiley, 1997, pp. 591–596.
6. W. Munk, P. Worcester, and C. Wunsch, *Ocean Acoustic Tomography*, Cambridge, UK: Cambridge Univ. Press, 1995.
7. G. V. Frisk, *Ocean and Seabed Acoustics: A Theory of Wave Propagation*, Englewood Cliffs, NJ: Prentice-Hall, 1994.
8. F. B. Jensen, W. A. Kuperman, M. B. Porter, and H. Schmidt, *Computational Ocean Acoustics*, New York: American Institute of Physics, 1994.
9. P. H. Dahl and J. W. Choi, Precursor arrivals in the Yellow Sea, their distinction from first-order head waves, and their geoacoustic inversion, *J. Acoust. Soc. Am.*, **129**: 3525–3533, 2006.
10. P. M. Morse and K. U. Ingard, Linear acoustic theory, in S. Flügge (ed.), *Handbuch der Physik*, Vol. XI/1, Berlin: Springer-Verlag, 1961.
11. P. M. Morse and K. U. Ingard, *Theoretical Acoustics*, New York: McGraw-Hill, 1968, reprint Princeton, NJ: Princeton Univ. Press, 1986.
12. A. P. Dowling and J. E. Ffowcs Williams, *Sound and Sources of Sound*, Chichester, UK: Ellis Horwood, 1983.
13. D. T. Blackstock, *Fundamentals of Physical Acoustics*, New York: Wiley, 2000.
14. H. Kuttruff, *Ultrasonics: Fundamentals and Applications*, Amsterdam: Elsevier, 1991.
15. C. S. Clay, and H. Medwin, *Acoustical Oceanography: Principles and Applications*, New York: Wiley, 1977.
16. V. M. Ristic, *Principles of Acoustic Devices*, New York: Wiley, 1983.
17. D. Stansfield, *Underwater Electroacoustic Transducers*, Bath and St. Albans, UK: Bath Univ. Press and Institute of Acoustics, 1991.
18. L. E. Kinsler, A. R. Frey, A. B. Coppens, and J. V. Sanders, *Fundamentals of Acoustics*, New York: Wiley, 1982.
19. R. J. Bobber, *Underwater Electroacoustic Measurements*, Los Altos, CA: Peninsula, 1988.
20. K. G. Foote, Maintaining precision calibrations with optimal copper spheres, *J. Acoust. Soc. Am.*, 1983, **73**: 1054–1063.
21. C. H. Sherman and J. L. Butler, *Transducers and Arrays for Underwater Sound*, New York: Springer, 2007.
22. J. A. Smith, Doppler sonar and surface waves: Range and resolution, *J. Atmos. Oceanic Technol.*, **6**: 680–696, 1989.
23. P. H. Dahl, On the spatial coherence and angular spreading of sound forward scattered from the sea surface: Measurements and interpretive model, *J. Acoust. Soc. Am.*, **100**: 748–758, 1996.
24. J. W. Choi and P. H. Dahl, Mid to High Frequency Bottom Loss in the East China Sea, *IEEE J. Oceanic Eng.*, **29**: 980–987, 2004.
25. J. R. Apel, *et al.*, An overview of the 1995 swarm shallow-water internal wave acoustic scattering experiment, *IEEE J. Oceanic Eng.*, 465–500, 1997.

26. S. M. Flatté, R. Dashen, W. H. Munk, K. Watson, and F. Zachariasen, *Sound Transmission Through a Fluctuating Ocean*, Cambridge, UK: Cambridge Univ. Press, 1979.
27. R. E. Francois and G. R. Garrison, Sound absorption based on ocean measurements. Part i: Pure water and magnesium sulfate contributions. Part ii: Boric acid contribution and equation for total absorption, *J. Acoust. Soc. Am.*, **72**: 896–907, 1982.
28. D. R. Jackson, K. B. Briggs, K. L. Williams, and M. D. Richardson, Tests of models for high-frequency seafloor backscatter, *IEEE J. Oceanic Eng.*, **21**: 458–470, 1996.
29. P. D. Mourad and D. R. Jackson, High frequency sonar equation models for bottom backscatter and forward loss, *OCEANS '89 Conf. Proc.*, 1989, pp. 1168–1175.
30. K. L. Williams and D. R. Jackson, Bistatic bottom scattering: Model, experiments, and model/data comparison, *J. Acoust. Soc. Am.*, **103**: 169–181, 1998.
31. P. H. Dahl and W. L. J. Fox, Measurement and interpretation of angular spreading from multiple boundary interactions in a shallow water channel, in N. G. Pace, *et al.* (eds.), *High Frequency Acoustics in Shallow Water*, La Spezia, Italy: 1997, pp. 107–114.
32. H. Medwin, *in situ* acoustic measurements of microbubbles at sea, *J. Geophys. Res.*, **82**: 971–976, 1977.
33. J. Dalen and A. Løvik, The influence of wind-induced bubbles on echo integration surveys, *J. Acoust. Soc. Am.*, **69**: 1653–1659, 1981.
34. S. A. Thorpe, On the clouds of bubbles formed by breaking wind-waves in deep water, and their role in air-sea gas transfer, *Philos. Trans. R. Soc. London A*, **304**: 155–210, 1982.
35. S. Vagle and D. M. Farmer, The measurement of bubble-size distributions by acoustical backscatter, *J. Atmos. Oceanic Technol.*, **9**: 630–644, 1992.
36. M. Gensane, Bubble population measurements with a parametric array, *J. Acoust. Soc. Am.*, **95**: 3183–3190, 1994.
37. P. H. Dahl and A. T. Jessup, On bubble clouds produced by breaking waves: An event analysis of ocean acoustic measurements, *J. Geophys. Res.*, **100**: 5007–5020, 1995.
38. P. H. Dahl, Bubble clouds and their transport within the surf zone as measured with a distributed array of upward-looking sonars, *J. Acoust. Soc. Am.*, **109**: 133–142, 2001.
39. H. Medwin, Acoustic fluctuations due to microbubbles in the near-surface ocean, *J. Acoust. Soc. Am.*, **56**: 1100–1104, 1974.
40. D. M. Farmer and S. Vagle, Waveguide propation of ambient sound in the ocean-surface layer, *J. Acoust. Soc. Am.*, **86**: 1897–1908, 1989.
41. K. W. Commander and A. Prosperetti, Linear pressure waves in bubbly liquids: Comparison between theory and experiments, *J. Acoust. Soc. Am.*, **85**: 732–746, 1989.
42. H. C. Pumphrey and L. A. Crum, Free oscillations of near-surface bubbles as a source of the underwater noise of rain, *J. Acoust. Soc. Am.*, **87**: 142–148, 1990.
43. P. A. Crowther and A. Hansla, The lifetimes, vortices and probable origins of sonic and ultrasonic noise sources on the sea surface, in B. B. Kerman, (ed.), *Natural Physical Sources of Underwater Sound*, Boston: Kluwer Academic, 1993, pp. 379–392.
44. P. H. Dahl, High frequency noise emitted from ocean breaking waves, in M. J. Buckingham andJ. R. Potter (eds.), *Sea Surface Sound '94: Third International Meeting on Natural Physical Processes Related to Sea Surface Sound*, New York: World Scientific Press, 1995, pp. 174–184.
45. S. Vagle and D. M. Farmer, A comparison of four methods for bubble size and void fraction measurements, *IEEE J. Oceanic Eng.*, **23**: 211–222, 1998.
46. J. W. Caruthers, S. J. Stanic, P. A. Elmore, and R. R. Goodman, Acoustic attenuation in very shallow water due to the presence of bubbles in rip currents, *J. Acoust. Soc. Am.*, 1999; **106**: 617–625.
47. E. Lamarre and W. K. Melville, Sound-speed measurements near the ocean surface, *J. Acoust. Soc. Am.*, 1994; **96**: 3605–3616.
48. O. A. Mathisen, Acoustic assessment of stocks of fish and krill, *Proc. 6th Conf. Comité Arct. Int. New York*, 1989, pp. 556–581.
49. D. Gaudet, Enumeration of migratory salmon populations using fixed-location sonar counters, *Rapp. P.-V. Reun., Cons. Int. Explor. Mer.*, **189**: 197–209, 1990.
50. M. V. Trevorrow, Detection of migratory salmon in the fraser river using 100-kHz sidescan sonars, *Can J. Fish. Aquat. Sci.*, **54**: 1619–1629, 1997.
51. D. V. Holliday and R. E. Pieper, Bioacoustical oceanography at high frequencies, *ICES J. Mar. Sci.*, **52**: 279–296, 1995.
52. A. Ishimaru, *Wave Propagation and Scattering in Random Media*, New York: Academic Press, 1978.
53. F. Masahiko, K. Ishii, and Y. Miyanohana, Attenuation of sound by schooling fish, *J. Acoust. Soc. Am.*, **92**: 987–994, 1992.
54. K. G. Foote, Importance of the swimbladder in acoustic scattering by fish: A comparison of gadoid and mackerel target strengths, *J. Acoust. Soc. Am.*, **67**: 2084–2089, 1980.
55. P. H. Dahl, and O. A. Mathisen, Measurement of fish target strength and associated directivity at high frequencies, *J. Acoust. Soc. Am.*, **73**: 1205–1211, 1983.
56. D. V. Holliday and R. E. Pieper, Volume scattering strengths in zooplankton distributions at acoustic frequencies between 0.5 and 3 MHz, *J. Acoust. Soc. Am.*, **67**: 135–146, 1980.
57. T. K. Stanton, C. S. Clay, and D. Chu Ray, representation of sound scattering by weakly scattering deformed fluid cylinders: Simple physics and application to zooplankton, *J. Acoust. Soc. Am.*, **94**: 3454–3462, 1993.
58. T. K. Stanton, D. Chu, P. H. Wiebe, and C. S. Clay, Average echoes from randomly oriented random-length finite cylinders: Zooplankton models, *J. Acoust. Soc. Am.*, **94**: 3463–3472, 1993.
59. R. Pinkel, Observations of strongly nonlinear internal motion in the open sea using a range-gated Doppler sonar, *J. Phys. Ocean.*, **9**: 675–686, 1979.
60. R. Pinkel, On the use of Doppler sonar for internal wave measurements, *Deep-Sea Res.*, **28**: 269–289, 1981.
61. A. J. Plueddemann and R. Pinkel, Characterization of the patterns of diel migration using a Doppler sonar, *Deep-Sea Res.*, **36**: 509–530, 1989.
62. L. Goodman, Acoustic scattering from ocean microstructure, *J. Geophys. Res.*, **95**: 11557–11573, 1990.
63. H. E. Seim, M. C. Gregg, and R. T. Miyamoto, Acoustic backscatter from turbulent microstructure, *J. Atmos. Oceanic Technol.*, **12**: 367–372, 1995.
64. T. K. Stanton, P. H. Wiebe, D. Chu, and L. Goodman, Acoustic characterization and discrimination of marine zooplankton and turbulence, *ICES J. Mar. Sci.*, **51**: 469–479, 1994.
65. O. A. Mathisen and M. C. Macaulay, The morphological features of a super swarm of krill, *Euphausia superba, Mem. Natl. Inst. Polar Res. Spec. Issue (Jpn.)*, (27), 153–164, 1983.

66. R. Pinkel, *et al.*, Solitary waves in the western equatorial Pacific Ocean, *Geophys. Res. Lett.*, **24**: 1603–1606, 1997.
67. D. R. Jackson, A. Baird, J. J. Crisp, and P. A. G. Thomson, High-frequency bottom backscatter measurements in shallow water, *J. Acoust. Soc. Am.*, **80**: 1188–1199, 1986.
68. P. H. Dahl, W. J. Plant, B. Nützel, A. Schmidt, H. Herwig, and E. A. Terray, Simultaneous acoustic and microwave backscattering from the sea surface, *J. Acoust. Soc. Am.*, **101**: 2583–2595, 1997.
69. P. H. Dahl and W. J. Plant, The variability of high-frequency acoustic backscatter from the region near the sea surface, *J. Acoust. Soc. Am.*, **101**: 2596–2602, 1997.
70. H. Matsumoto, R. Dziak, and C. G. Fox, Estimation of seafloor microtopographic roughness through modeling of acoustic backscatter data recorded by multibeam sonar systems, *J. Acoust. Soc. Am.*, **94**: 2777–2787, 1993.
71. D. R. Jackson, K. L. Williams, and K. B. Briggs, High-frequency acoustic observations of benthic spatial and temporal variability, *Geo-Marine Lett.*, **16**: 212–218, 1996.
72. E. O. Belcher, Application of thin, acoustic lenses in a 32-beam, dual-frequency, diver-held sonar, *OCEANS '96 MTS/IEEE Conf. Proc.*, 1996, pp. 767–772.
73. E. O. Belcher, B. Matsuyama, and G. M. Trimble, Object Identification with Acoustic Lenses, *Conference Proceedings MTS/IEEE Oceans 2001, Volume 1, Session 1*, Honolulu Hawaii, 2001, pp. 6–11.

PETER H. DAHL
Applied Physics Laboratory
University of Washington
Seattle, Washington